Nano Research

ISSN 1998-0124 CN 11-5974/O4
https://doi.org/10.26599/NR.2026.94908837

Research Article

Templating openness engineering: A strategy for performance enhancement via synergistic nanocrystalline-amorphous composite in solution-processed InO_x/PEG TFTs

Zhennan Zhu[1], Wei Lv[1], Xiaojiao Kang[1], Jialing Sun[1], Xuemei Chen[1], Qiwen Pan[1], Rihui Yao[2], Hongcheng Wang[1](✉), Honglong Ning[2,3](✉)

[1] School of Electrical Engineering and Intelligentization, Dongguan University of Technology, Dongguan 523808, China

[2] Guangdong Basic Research Center of Excellence for Energy & Information Polymer Materials, State Key Laboratory of Luminescent Materials and Devices, School of Materials Sciences and Engineering, South China University of Technology, Guangzhou 510640, China

[3] The International School of Microelectronics, Dongguan University of Technology, Dongguan 523808, China

Nano Res., **Just Accepted Manuscript** • https://doi.org/10.26599/NR.2026.94908837

https://www.sciopen.com/journal/1998-0124 on May. 11, 2026

Just Accepted

Template for Preparation of Manuscripts for *Nano Research*

This template is to be used for preparing manuscripts for submission to *Nano Research*. Use of this template will save time in the review and production processes and will expedite publication. However, use of the template is not a requirement of submission. Do not modify the template in any way (delete spaces, modify font size/line height, etc.). If you need more detailed information about the preparation and submission of a manuscript to Nano Research, please see the latest version of the Instructions for Authors at https://www.sciopen.com/journal/1998-0124.

TABLE OF CONTENTS (TOC)

Authors are required to submit a graphic entry for the Table of Contents (TOC) in conjunction with the manuscript title. This graphic should capture the readers' attention and give readers a visual impression of the essence of the paper. Labels, formulae, or numbers within the graphic must be legible at publication size. Tables or spectra are not acceptable. Color graphics are highly encouraged. The resolution of the figure should be at least 600 dpi. The size should be at least 50 mm × 80 mm with a rectangular shape (ideally, the ratio of height to width should be less than 1 and larger than 5/8). One to two sentences should be written below the figure to summarize the paper. To create the TOC, please insert your image in the template box below. Fonts, size, and spaces should not be changed.

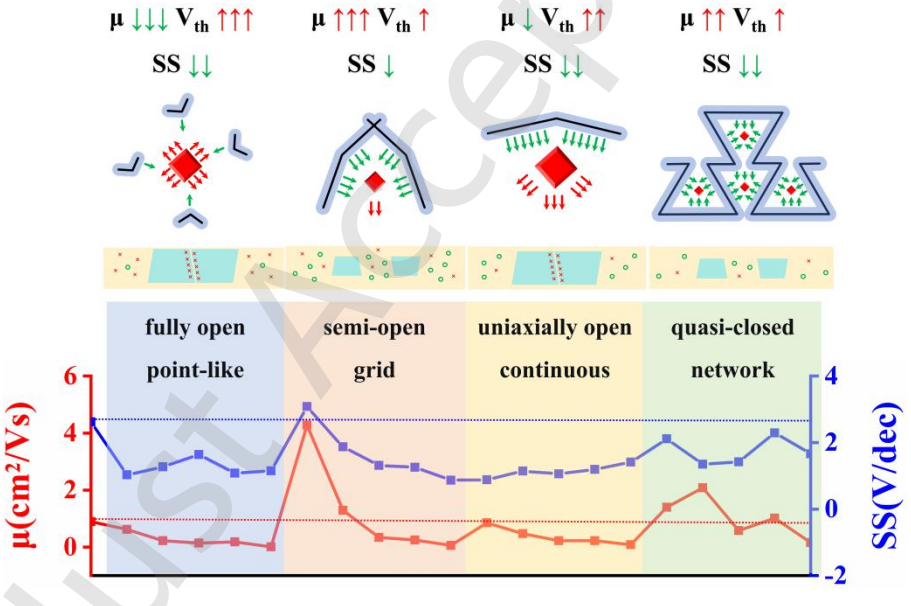

Programming PEG chain length defines a continuous template openness spectrum from semi-open grid to quasi-closed network, enabling either exceptional peak mobility or robust performance over a wide concentration range for printed oxide/polymer TFTs.

Nano Research

Open Access

Research Article

Templating openness engineering: A strategy for performance enhancement via synergistic nanocrystalline-amorphous composite in solution-processed InO_x/PEG TFTs

Zhennan Zhu[1], Wei Lv[1], Xiaojiao Kang[1], Jialing Sun[1], Xuemei Chen[1], Qiwen Pan[1], Rihui Yao[2], Hongcheng Wang [1]✉, and Honglong Ning [2, 3]✉

[1] *School of Electrical Engineering and Intelligentization, Dongguan University of Technology, Dongguan 523808, China*
[2] *Guangdong Basic Research Center of Excellence for Energy & Information Polymer Materials, State Key Laboratory of Luminescent Materials and Devices, School of Materials Sciences and Engineering, South China University of Technology, Guangzhou 510640, China*
[3] *The International School of Microelectronics, Dongguan University of Technology, Dongguan 523808, China.*

Received: 6 April 2026; **Revised:** 24 April 2026; **Accepted:** 11 May 2026

✉Address correspondence to Hongcheng Wang, wanghc@dgut.edu.cn; Honglong Ning, ninghl@scut.edu.cn

Cite this article: *Nano Research*, 2026, 19, 94908837 https://doi.org/10.26599/NR.2026.94908837

ABSTRACT: Metal oxide semiconductors offer high mobility and solution processability but suffer from brittleness. Polymer blending is a promising route to flexibility, yet the role of polymer chain segment distribution in microstructure control remains poorly understood. Here we introduce a "templating openness" strategy by systematically varying polyethylene glycol (PEG) chain length. Using multi-scale characterization including MD simulations, UV-vis, TEM, XPS, and TFT measurements, we reveal that PEG chains in solution define a continuous template spectrum from fully open to quasi-closed. Short chains create disordered obstacle fields, degrading mobility. Long chains form single continuous obstacles, yielding oriented grains but mediocre performance. Medium-length chains self-assemble into semi-open grids, guiding fine uniform nanocrystals within a high-quality amorphous matrix that suppresses deep traps and enriches shallow donors, boosting mobility from 0.89 to 4.28 cm^2/Vs. Ultra-long chains form quasi-closed network cavities, enabling stable defect chemistry and robust enhancement across a wide concentration window. This work establishes a complete structure-property framework linking templating openness to device performance, providing a new paradigm for metal oxide/polymer semiconductor design based on physical chain-length regulation.

KEYWORDS: metal oxide/polymer composites, solution-processed TFTs, templating openness, structure-property relationship, flexible electronics

1 Instruction

The rapid development of wearable electronics, flexible displays, and the Internet of Things has positioned printed electronics as a key technology due to its advantages in large-area, low-cost manufacturing[1-3]. Among printed functional devices, thin-film transistors (TFTs) serve as core components for signal amplification and switching, making the development of semiconductor materials that combine high electrical performance with solution processability a critical research focus[4-6]. Oxide semiconductors, particularly indium oxide (InO_x), are promising TFT channel materials owing to their high electron mobility, optical transparency, and solution compatibility[7-8]. However, the intrinsic rigidity and brittleness of oxides render them susceptible to microcrack formation under mechanical bending, severely limiting their application in flexible electronics[9-11]. Achieving high mobility while imparting mechanical flexibility remains a central challenge.

Oxide/polymer composites offer a promising route to address this challenge, and existing studies can be categorized into several representative strategies. Divya et al. used polymers immiscible with indium oxide to induce heterogeneous nucleation via phase separation, achieving excellent bending stability (no degradation at 1.5 mm radius) while maintaining high mobility (40-45 cm^2/Vs)[12]. Yu et al. introduced poly(4-vinylphenol) (PVP) into the oxide matrix to suppress crystallization and induce amorphization, improving flexibility at the cost of monotonically decreasing mobility[13]. Kim et al. also demonstrated that incorporating insulating polymers (PVPh, PHEMA) into ZnO precursor solutions via bulk blending induces surface wrinkling and achieves high mobility (63.7 cm^2/Vs) in electrolyte-gated transistors after thermal annealing[14]. Huang et al. and Lee et al. exploited the electron-donating ability of amine-containing or conductive polymers to modulate carrier concentration and microstructure via chemical doping, achieving significant mobility enhancement under optimized conditions[15-17]. Huang et al. further demonstrated that polyvinyl alcohol (PVA) can act as a hydrogen dopant in indium gallium oxide, converting six-coordinate Ga to four-coordinate Ga and suppressing deep traps, thereby enhancing mobility by over 70-fold[18]. Additionally, Song et

al. demonstrated a surface doping strategy by coating polyvinyl alcohol (PVA) onto solution-processed tin oxide TFTs to modulate carrier concentration and passivate devices, which, though not a true oxide/polymer composite approach, still offers valuable reference significance, further illustrating the versatility of polymer-based approaches in oxide semiconductor engineering[19]. These studies collectively demonstrate the potential of polymer incorporation to improve oxide TFT performance. However, most approaches rely on specific polymer chemical properties such as immiscibility, electron-donating capability, or surface functionalization.

Most recently, our group systematically investigated the role of polyacrylamide (PAM) molecular weight in InO_x/PAM composite TFTs, revealing that PAM chain length governs the morphology and distribution of nanocrystalline domains, enabling synergistic regulation of carrier transport pathways[20]. Here, we go beyond such polymer-specific observations by proposing a universal mechanism based on the spatial occupancy mode of polymer chains, which we term "template openness". Defined as the spatial distribution pattern of polymer segments in solution, this concept creates a continuous template spectrum from "fully open" to "quasi-closed" that guides precursor nucleation and growth, enabling synergistic optimization of nanocrystal size, crystallinity, amorphous matrix quality, and defect chemistry. Compared to strategies relying on specific chemical interactions, this physically based templating approach offers broader applicability. To validate this mechanism, we select polyethylene glycol (PEG) as a model polymer due to its water solubility, simple structure, and precisely tunable chain length. Importantly, the terminal hydroxyl groups of PEG exhibit minimal chemical interference with In^{3+}, allowing it to function primarily as a physical template[21-22]. Four PEGs with molecular weights of 4 kDa, 35 kDa, 100 kDa, and 5000 kDa are chosen, covering a range from oligomers to ultra-high molecular weight polymers, with concentration gradients of 1-5 wt% for each. The pristine indium oxide sample is denoted as MO, while the polymer-blended samples are referred to as MOP4k, MOP35k, MOP100k, and MOP5M, with the concentration indicated by a suffix (e.g., MOP4k-1%). Using multi-scale characterization including molecular dynamics simulations, UV-vis spectroscopy, FIB-TEM, XPS, and TFT electrical measurements, we establish a complete chain of evidence from solution structure to solid-state film morphology to device performance. Our results demonstrate that under optimized template openness, composite film TFT mobility is significantly enhanced compared to pristine InO_x devices, validating this physical chain-length regulation strategy.

2 Experimental section

2.1 Materials Selection and Composite Solution Preparation

Indium oxide precursor solution was prepared using indium nitrate hydrate ($In(NO_3)_3 \cdot xH_2O$, Macklin Inc.) as the indium source and deionized water as the solvent. Four polyethylene glycol (PEG) samples with different molecular weights were selected: PEG-4k (average Mw=4 kDa), PEG-35k (average Mw=35 kDa), PEG-100k (average Mw=100 kDa), and PEG-5M (average Mw=5000 kDa). All PEG samples possess linear structures with hydroxyl terminal groups. PEG-4k, PEG-35k, PEG-100k, and PEG-5M were all purchased from Macklin Inc. Prior to use, all PEG samples were dried in a desiccator for 12 h to remove adsorbed moisture.

First, an appropriate amount of indium nitrate hydrate was weighed and placed in a clean glass vial. Calculated amount of deionized water was added, and the mixture was magnetically stirred at room temperature for 10 min until complete dissolution, forming a transparent solution with a concentration of 0.1 mol/L. Predetermined mass of dried PEG sample was dissolved in the resulting solution under stirring at room temperature for 20 min until fully dissolved, yielding a homogeneous and transparent composite solution. For each PEG molecular weight, five concentration gradients of 1 wt%, 2 wt%, 3 wt%, 4 wt%, and 5 wt% (with respect to the mass of indium oxide equivalent to the molar amount of indium nitrate) were prepared to systematically investigate the concentration effects. Finally Fluorocarbon surfactant (FSO) was added at a concentration of 0.05 wt% (based on deionized water) to improve the wettability of solution, and the solution were stirred for 5 min. All composite solutions were used within 24 h after preparation to avoid hydrolysis-condensation reactions caused by prolonged storage. Prior to use, the solutions were filtered through 0.45 μm aqueous membrane filters to remove possible particulate impurities.

2.2 Film and device fabricating

Glass substrates pre-patterned with Mo bottom-gate electrode (thickness 200 nm) and SiN_x/SiO_x composite gate insulator (thickness 250/50 nm, capacitance density 1.7×10^{-4} F/m^2) were used. The composite semiconductor films were deposited by spin-coating (LEBO Science, EZ4 SPIN COATER) at 5000 rpm for 25 s to form uniform wet films. After spin-coating, the wet films were annealed on a hot plate at 215 °C for 30 min in ambient air to remove residual solvents and physically adsorbed water, and to promote nitrate decomposition, In-O-In network condensation and crystallization. Thin-film transistors were fabricated with a bottom-gate top-contact configuration. On the substrates with the semiconductor layers, Mo source/drain electrodes with a thickness of 80 nm were deposited by sputtering. Patterning of the source/drain electrodes was achieved using stainless steel shadow masks. The channel width (W) was 800 μm, and the channel lengths (L) were 100, 200, 300, 400, and 500 μm, corresponding to W/L ratios of 8, 4, 2.67, 2, and 1.6, respectively.

2.3 Characterization

UV-vis absorption spectra of the composite solutions were recorded using a spectrophotometer (MAPADA, UV-6100S) over a scanning range of 200-800 nm. Liquid samples were placed in quartz cuvettes with deionized water as the reference. Chemical state analysis of the films was performed by X-ray photoelectron spectroscopy (Thermo Fisher, ESCALAB XI$^+$). Nanostructural characterization of the films was conducted using transmission electron microscopy (JEOL, JEM-F200), with samples prepared by in situ focused ion beam technique (Hitachi, NX5000). Grain identification and statistical analysis: at least eight TEM images from different regions were acquired for each sample. Grain boundaries were manually identified using ImageJ software, and the crystalline area fraction, grain number density, average equivalent diameter, and distribution of grain boundary normal vectors were calculated. Electrical performance of the TFTs was measured using a semiconductor parameter analyzer (Keithley, 4200A-SCS)

under ambient conditions at room temperature. Transfer characteristics were measured by sweeping V_{GS} from -80 V to +80 V at V_{DS} = 30 V (saturation regime). Output characteristics were measured by sweeping V_{DS} from 0 V to +30 V at V_{GS} = 30 V. At least 15 devices were tested for each condition, and performance parameters are reported as average values.

2.4 Molecular Dynamics Simulations

Molecular dynamics simulations were performed using the Forcite module in the Materials Studio software package (BIOVIA, licensed to South China University of Technology), with the Dreiding force field. This general-purpose all-atom force field can reasonably describe the non-bonded interactions among polymers, water molecules, and inorganic ions. The simulated systems contained four components: PEG chains, In^{3+} ions, NO_3^- ions, and water molecules. Force fields such as COMPASS were not employed due to the lack of parameters for indium ions. Considering the low polymer concentration in real solutions, modeling at the actual ratio would make it difficult to observe effective chain–ion interactions within the available computational resources. Therefore, a "concentrated micro-region" model strategy was adopted: while maintaining the realistic ratios of water and precursors, the polymer content was amplified to ensure the presence of at least one polymer chain per simulation system. Accordingly, the simulation results reflect the dynamic behavior of components in the vicinity of polymer chains in a dilute solution. To compare the effect of polymer molecular weight on component dynamics under similar total ethylene glycol (EG) unit counts, three systems were constructed: MOP4k (20 chains, each with 100 EG units), MOP35k (3 chains, each with 800 EG units), and MOP100k (1 chain with 2000 EG units). Each system contained the same numbers of In^{3+} (20), NO_3^- (60), and water molecules (10,000). The MOP5M system could not be simulated due to the software's EG unit limit of 2000. The simulation protocol consisted of: (1) energy minimization using the Smart algorithm with a convergence criterion of 0.001 kcal/mol/Å; (2) 200 ps NVT heating from 10 K to 298 K with the Nose–Hoover thermostat; (3) 300 ps NPT equilibration at 298 K and 1 atm using the Berendsen barostat; and (4) 50 ns NPT production run at 298 K and 1 atm with a time step of 1 fs, saving trajectories every 5 ps. Non-bonded interactions were treated with a van der Waals cutoff of 15.5 Å and PPPM electrostatics. From the production trajectories, the radius of gyration (R_g) distribution of PEG chains, radial distribution functions (RDFs), and diffusion coefficients (D) of In^{3+} ions (obtained by linear fitting of the mean square displacement) were calculated.

3 Results and discussion

3.1 Segmental Spatial Distribution and Template Characteristics in Solution

To elucidate how PEG molecular weight governs its intrinsic characteristics as a spatial template at the atomic scale, we performed all-atom molecular dynamics simulations on three representative systems, MOP4k, MOP35k, and MOP100k, with corresponding solution models constructed as shown in Figure 1a. Under comparable total EG units, the three systems correspond to 20 short chains (MOP4k), three medium-length chains (MOP35k), and one long chain (MOP100k), respectively, directly translating molecular weight differences into coupled variations in chain number and length. All relevant physical quantities of each system reached a well-converged state within the 50 ns production run. Analysis of the radius of gyration distributions reveals the conformational characteristics of PEG chains in solution (Figure 1b). MOP4k exhibits a broad continuous distribution (14-22 Å), reflecting a highly dispersed scattered obstacle field from 20 independently moving short chains. MOP100k displays three connected sharp peaks confined to 93-95 Å, indicating a single long chain with relatively fixed conformation occupying a large continuous region. Notably, MOP35k exhibits three distinct peaks at 50, 60, and 70 Å, each composed of sub-peaks, demonstrating that the three chains remain spatially independent without excessive entanglement, each maintaining a well-defined conformational state.

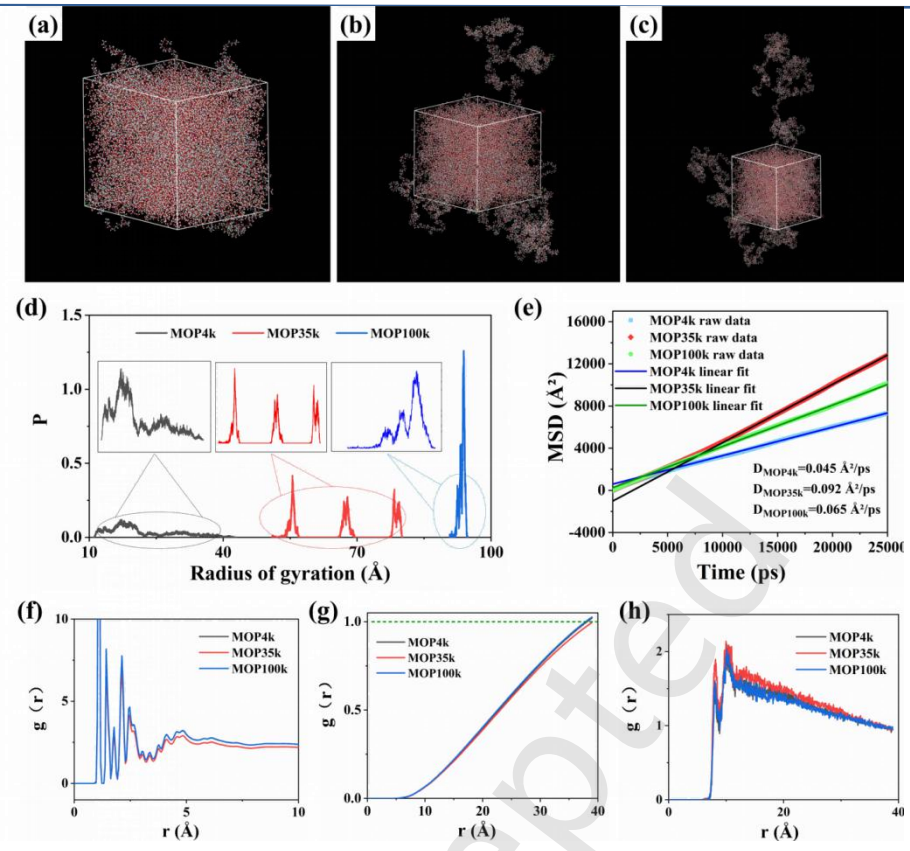

Figure 1 Simulation box snapshots of the (a) MOP4k (20 chains), (b) MOP35k (3 chains), and (c) MOP100k (1 chain) systems. (d) Radius of gyration (R_g) distribution curves of PEG chains in the three systems. (e) Mean square displacement (MSD) of In^{3+} ions as a function of time with linear fits used to calculate diffusion coefficients. (f) Total radial distribution function centered on PEG atoms, Total(PEG). (g) Radial distribution function centered on PEG atoms specifically for In^{3+} ions, Total(PEG-In). (h) Total radial distribution function centered on In^{3+} atoms, Total(In)

Radial distribution functions provide multiple perspectives on solution microstructure. The Total(PEG) curves, with PEG atoms as the reference center (Figure 1c), show perfect overlap for the first four sharp peaks in the 0-2.2 Å range, corresponding to intramolecular covalent bonds and strong hydrogen bonds within PEG. However, in the 2.5–40 Å range, the g(r) values for MOP35k are consistently lower than those for MOP4k and MOP100k, indicating that from the PEG segment perspective, the average density of surrounding atoms is lower in the MOP35k system. This subtle difference reflects that, under comparable total EG units, the three chains in MOP35k adopt a grid-like spatial occupation pattern with unoccupied regions between grid units, while the 20 short chains (dispersed distribution) in MOP4k and the single long chain (continuous agglomeration) in MOP100k both result in higher atomic density. The Total(PEG-In) curves, characterizing In^{3+} distribution with PEG atoms as reference (Figure 1d), exhibit g(r)=0 within 0-6 Å, demonstrating that PEG segments and In^{3+} never approach within 6 Å and are always separated by at least one water layer[23]. This confirms that PEG ether oxygens cannot interact directly with In^{3+}, establishing the predominantly physical nature of the interaction. At approximately 39 Å, all three curves approach unity, but a subtle difference persists: MOP35k is closer to 1, while MOP4k and MOP100k are slightly greater than 1 (≈1.02). Although MOP4k and MOP100k exhibit markedly different chain conformations, both form continuous coverage type obstacle fields—the former with obstacles everywhere, the latter as a single continuous obstacle—leading to weak ion accumulation at certain distances. In contrast, the grid-like structure of MOP35k with discrete coverage provides free regions for ions, resulting in more uniform distribution. The Total(In) curves, with In^{3+} as reference center (Figure 1e), exhibit two distinct peaks at 8 Å and 11 Å, assigned to the first and second hydration shells of In^{3+} based on visual evidence of water molecules surrounding In^{3+}. The In^{3+}-water distances obtained here exceed literature values (2.1 Å/4.1 Å)[24], possibly due to lack of specific parameterization for In^{3+} hydration in the Dreiding force field and perturbation by the high-concentration PEG environment[25]. Nevertheless, the relative differences carry clear physical meaning: MOP35k exhibits significantly higher g(r) values at both peaks compared to MOP4k and MOP100k, demonstrating more complete and less perturbed In^{3+} hydration structure, corroborating that the grid-like structure provides a relatively free spatial environment for ions.

The calculated diffusion coefficients reveal non-monotonic behavior in solute dynamics (Figure 1f). In^{3+} diffusion coefficients follow the order D_{35k} (0.092) > D_{100k} (0.065) > D_{4k} (0.045) (Å²/ps), demonstrating that diffusion is not monotonically related to molecular weight but reflects the impact of obstacle field topology on ionic motion resistance. In the dispersed obstacle field of MOP4k, 20 short chains densely distributed and continuously moving create a high-frequency disordered collision field that frequently interrupts ionic trajectories, yielding the lowest diffusion coefficient. In the single continuous obstacle field of MOP100k, ions must navigate around a large obstacle, requiring longer detour paths and resulting in moderate diffusion. In the grid-like structure of MOP35k, chains concentrated at discrete locations form unobstructed diffusion channels between them, allowing ions to move without frequent collisions or long detours, yielding the highest diffusion coefficient.

In summary, molecular dynamics simulations reveal that under comparable total EG units, molecular weight programs the spatial distribution pattern of PEG segments in solution by determining chain number and length. MOP4k forms a continuously dispersed obstacle field, MOP100k forms a single continuous obstacle field, and MOP35k forms a grid-like structure with discrete coverage. These distribution differences directly modulate the local environment and dynamic behavior of In^{3+}: discrete coverage provides free space for ions, resulting in complete hydration shells and fastest diffusion, while continuous coverage modes lead to ionic accumulation, perturbed hydration shells, and hindered diffusion. These findings provide molecular-scale evidence for understanding the differentiated template roles of PEG with varying molecular weights in subsequent film formation.

3.2 Polymer Molecular Weight Controlled Precursor Aggregation

To investigate how PEG molecular weight and concentration influence the aggregation state of indium oxide precursors in solution, we performed UV-vis absorption spectroscopy on pure MO and all composite solution systems (Figure 2). The pure MO solution exhibits a characteristic absorption peak at 300 nm, attributed to the ligand-to-metal charge transfer transition between In^{3+} ions and their coordinated oxygen atoms (Figure S1)[26-27]. The intensity of this peak is highly sensitive to the local coordination environment and aggregation state of the precursor species[28]. Upon PEG incorporation, the concentration-dependent behavior of the 300 nm peak exhibits pronounced molecular weight differentiation, closely corresponding to the segmental spatial distribution patterns revealed by molecular dynamics simulations.

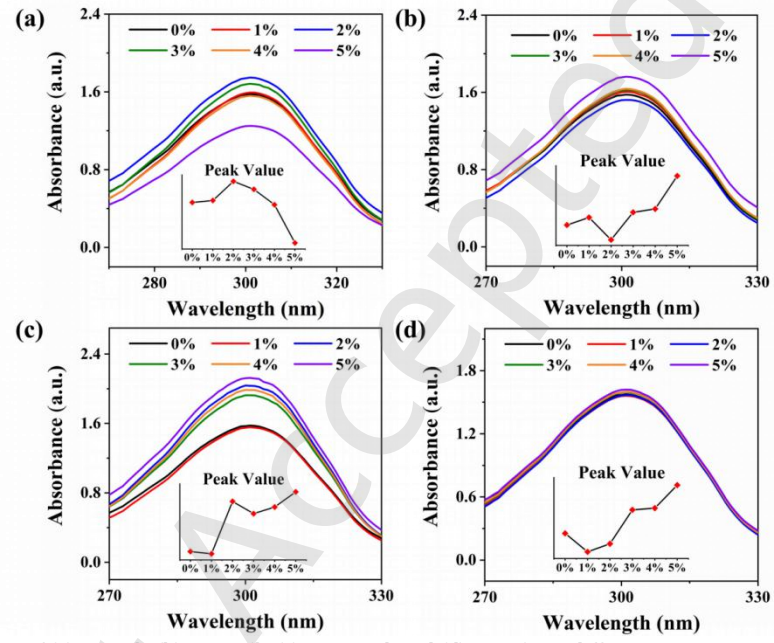

Figure 2 UV spectra of (a) MOP4k, (b) MOP35k, (c) MOP100k and (d) MOP5M at different PEG concentrations (1-5 wt%).

For the MOP4k system, absorbance first increases within 0-2 wt% and then decreases markedly above 3 wt%. Combined with the continuous dispersed obstacle field depicted in MD simulations, this behavior indicates that at low concentrations, numerous short chains provide heterogeneous interfaces that mildly facilitate local precursor ordering. However, at high concentrations, the omnipresent short chains constitute a highly crowded obstacle field that hinders condensation kinetics through frequent spatial perturbations, disrupting pre-aggregates and driving the solution toward disorder. The absorbance decrease at high concentrations thus reflects the detrimental interference of the continuous dispersed obstacle field on ordered precursor condensation.

The MOP35k system exhibits distinctly different behavior: absorbance increases significantly within 0-1 wt%, followed by irregular fluctuations in the 1-3 wt% range and gradual recovery after 3 wt%. The 0-1 wt% absorbance increase is the most distinctive signature of this system. MD simulations indicate that the three medium-length chains adopt a discrete coverage mode, forming locally enriched grid-like structures with large open areas between grids. At very low concentrations, this structure provides a perturbation-free microenvironment, enabling formation of high-quality pre-aggregates and enhancing absorption. Above 1 wt%, increased grid density may cause structural crowding, complicating the pre-aggregate environment and causing fluctuations. The recovery after 3 wt% may relate to homogenization effects from the continuous polymer phase at high concentrations, allowing precursors to regain a stable confined environment.

The MOP100k system contrasts sharply with MOP35k: absorbance gradually decreases within 0-1 wt%, with values at 0 wt% and 1 wt% significantly lower than at higher concentrations, followed by irregular patterns in the 1-3 wt% range and gradual recovery after 3 wt%. MD simulations reveal that the single long chain maintains a relatively fixed conformation, forming a single continuous obstacle field. At very low concentrations, this single obstacle has limited influence and may mildly inhibit active species formation due to spatial occupation, resulting in lower absorbance. Only when concentration increases sufficiently (>1 wt%) does its spatial exclusion effect become significant, forcing precursor enrichment through strong physical confinement and causing absorbance recovery. Fluctuations in the 1-3 wt% range reflect the non-uniform regulation by this rigid template, which cannot organize precursors as finely as MOP35k and can only passively compress them by increasing occupied volume.

The MOP5M system exhibits yet another pattern:

behavior in the 0-1 wt% range resembles MOP100k (absorbance decrease), but the 2-5 wt% range shows continuous gradual increase. As an ultra-long chain, PEG-5M tends to form a pervasive transient network structure, constituting a quasi-closed network chamber template. At low concentrations, this network is not well-developed and imposes limited constraints. As concentration increases, network density grows, and its spatial confinement effect continuously strengthens, forcing precursors to uniformly enrich within network chambers and leading to steady absorbance increase. Unlike MOP100k, the network structure of MOP5M exhibits better isotropy and continuity, avoiding fluctuations and showing monotonic enhancement.

In summary, the UV spectra reveal that PEG regulates precursor aggregation states through synergistic effects of its segmental spatial distribution pattern and concentration. These solution-scale behaviors correspond well with MD simulation results, providing direct experimental evidence for understanding the differentiated template roles of PEG with varying molecular weights in subsequent film formation.

3.3 Solid-State Film Structures Directed by Template Openness

Previous studies have demonstrated that PEG can act as an effective structure-directing agent or template in the synthesis of indium-based oxide materials, enabling controlled modulation of particle morphology, size, and crystallinity[29-30]. Integrating the segmental spatial distribution patterns from molecular dynamics simulations with the precursor aggregation responses from UV-vis spectroscopy, we propose a mechanistic framework centered on the concept of template openness. This framework posits that under comparable total EG units, molecular weight programs the spatial topology of PEG segments in solution by determining chain number and length, and these distinct topologies guide precursors to evolve into fundamentally different solid-state thin film structures during spin-coating (shown in Figure 3):

① MOP4k forms a continuously dispersed obstacle field, representing a fully open, point-like template. The broad radius of gyration distribution and absorbance decrease at high concentrations indicate that although this template provides numerous heterogeneous nucleation sites, its ubiquitous, continuously moving segments create a high-frequency disordered collision environment. Precursors nucleate randomly without effective spatial guidance or confinement, leading to broadly distributed grain sizes, random orientations, and grains isolated by amorphous matrix. Grains grow excessively due to disordered competition, while amorphous regions become porous and defect-rich from frequent perturbations during condensation.

② MOP35k forms a discretely covered grid-like structure, constituting a semi-open multi-chain grid template. The three distinct radius of gyration peaks demonstrate well-defined chain conformations and spatial correlation, while the 0-1 wt% absorbance increase indicates efficient precursor guidance at very low concentrations. Segments concentrate at grid nodes, leaving large open areas between grids and creating a topology where multi-directional spatial constraints coexist with isotropic free channels. Grid nodes induce high-density uniform nucleation, grid boundaries provide moderate grain growth confinement, and open areas reserve perturbation-free microenvironments for dense condensation of intergranular amorphous matrix. This template is expected to yield fine uniform grains tightly connected by amorphous matrix, with grain size controlled by multi-directional confinement and amorphous regions undergoing ordered condensation with low defect density.

③ MOP100k has a chain distribution density approximately one-third that of MOP35k at equivalent mass, significantly reducing the probability of forming multi-chain grid templates. It thus tends to form a single continuous obstacle field, representing a uniaxially open linear continuous template. The concentrated radius of gyration distribution indicates an extended chain existing as a single continuous object. The UV-vis threshold behavior—decreased absorbance at low concentrations and recovery at high concentrations—reflects that a concentration threshold is required for significant spatial effects. This template features a large continuous obstacle forcing precursor alignment along its periphery, but provides only unidirectional guidance and limited confinement. It is expected to form relatively large grains with orientation along the template direction, but with insufficiently optimized intergranular connection regions and uneven amorphous matrix quality due to template rigidity and spatial asymmetry.

④ MOP5M forms quasi-closed network chambers, representing a highly confined continuous network template. The continuously increasing absorbance with concentration reflects isotropic strong physical confinement on precursors. This template partitions precursors within numerous micro-chambers, strongly inhibiting long-range diffusion and large-scale crystalline growth. It is expected to form thin films dominated by a uniform dense amorphous phase with minimal crystalline phases of limited size, where grain development is hindered by global confinement and the amorphous matrix becomes dense and homogeneous due to network constraints.

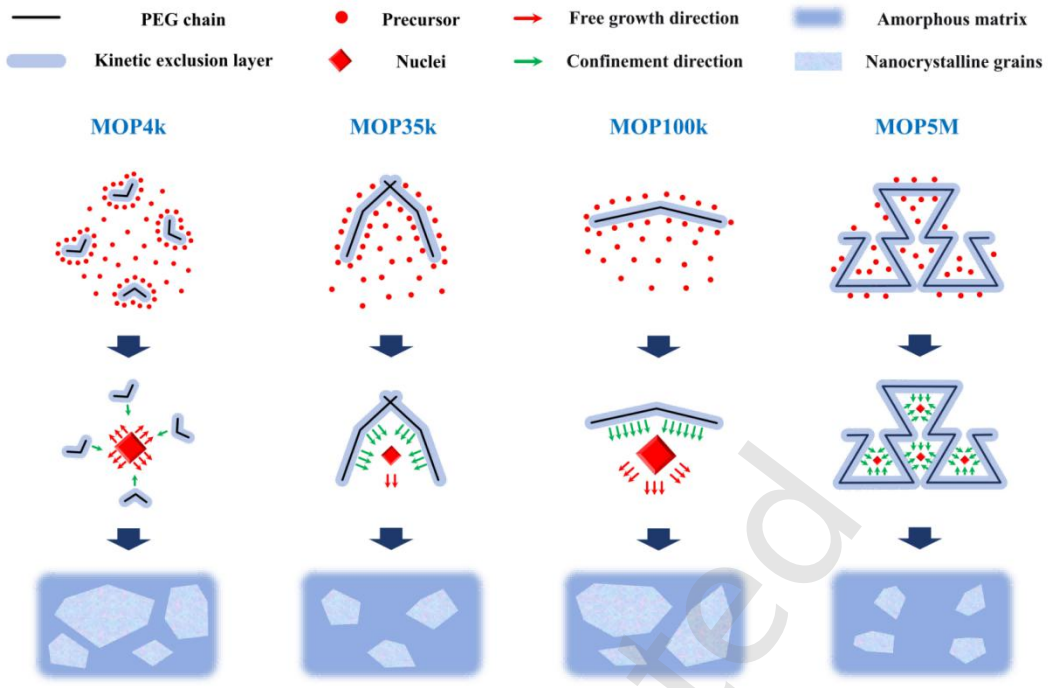

Figure 3 Schematic illustration of the PEG molecular weight-dependent template openness and its guidance on precursor distribution and grain growth.

The four PEG molecular weights define a continuous spectrum of templates from fully open to quasi-closed through their segmental spatial topologies. This framework establishes a theoretical correlation between solution-scale segmental distribution patterns and the ultimate structural characteristics of solid-state thin films.

To validate the predictions of the template openness model predicted from solution-phase behaviors, we performed cross-sectional TEM on pure MO and all composite films, with systematic statistical analysis of crystallized area fraction, grain number density, average equivalent diameter, and orientation distribution. These statistical data were derived from manually identified images presented in Figure S2-S6. MO films exhibit a textured crystallization characteristic arising from intrinsic thermodynamic driving forces rather than external template guidance. The crystallized area fraction is approximately 13%, with about 1.4 grains per image and a mean grain diameter of 2.7 nm. The orientation distribution is relatively concentrated rather than random, originating from the combined effects of two-dimensional confinement by the ultrathin film thickness (≈5 nm) and substrate interfacial energy. This serves as a baseline reference for evaluating polymer template effects.

The microstructure of MOP4k closely corresponds to its continuously dispersed obstacle field template. The crystallized area fraction increases markedly to 39%, grain size enlarges to 4.0 nm, grain count increases to about 3.5 per image, and the orientation distribution becomes the most broadened and dispersed among all systems. This substantial broadening directly demonstrates that the template disrupts the intrinsic thermodynamic orientation preference. Although the numerous short chains provide abundant heterogeneous nucleation sites, their ubiquitous presence and continuous motion create a disordered collision environment that randomizes grain growth directions.

MOP35k exhibits structural characteristics perfectly aligning with the discrete coverage grid template. The crystallized area fraction is approximately 11%, comparable to MO, but grain size is significantly reduced to 2.3 nm, grain count increases to about 1.7 per image, and the orientation distribution is moderately broadened. This combination of low crystallinity, fine grains, and moderate orientation broadening provides direct evidence for spatial partitioning guidance by the grid template: grid nodes induce high-density nucleation, while grid boundaries impose synergistic multi-directional confinement on grain growth, strictly controlling grain sizes. The open areas between grids enable ordered condensation of the amorphous matrix, forming a continuous, dense connecting phase. The moderate broadening indicates multi-directional constraints without enforcing a single preferred orientation, favorable for isotropic carrier transport. This contrasts with both the concentrated baseline of pure MO (thermodynamic preference) and the extreme broadening of MOP4k (randomizing disorder), positioning the grid template as a balanced guiding mechanism.

The structural characteristics of MOP100k reflect the single continuous obstacle field template. The crystallized area fraction reaches 39%, grain size is 4.5 nm, with about 2.3 grains per image, and the orientation distribution exhibits the highest concentration among all composite systems. This concentrated orientation originates from a fundamentally different mechanism than that of pure MO: the rigid, continuous obstacle forces uniaxial grain alignment along its direction. The high crystallinity and large grain size indicate that this guidance is unidirectional rather than multi-directional—grains can still grow freely in perpendicular directions.

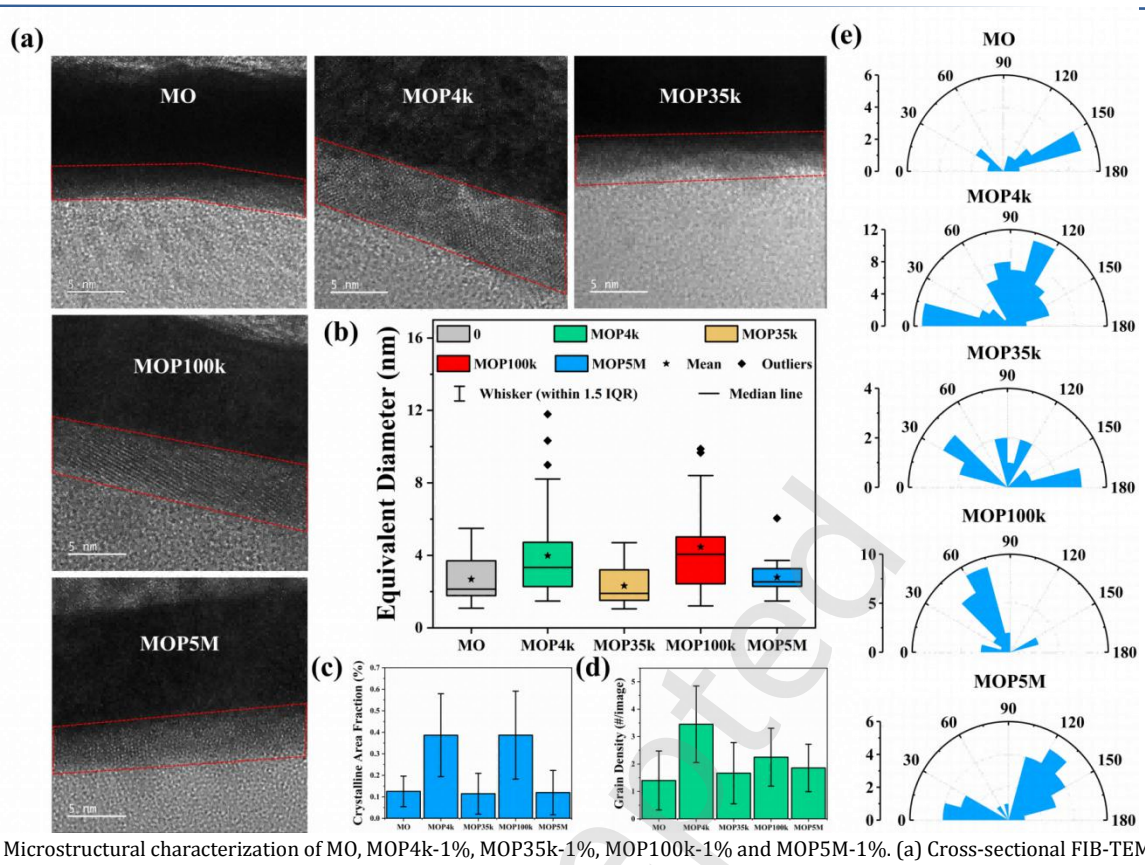

Figure 4 Microstructural characterization of MO, MOP4k-1%, MOP35k-1%, MOP100k-1% and MOP5M-1%. (a) Cross-sectional FIB-TEM images showing the film morphology; (b) Box plots of the average equivalent diameter of the crystal grains; (c) Crystallinity expressed as the area fraction of crystalline regions determined from the TEM images; (d) Grain number density per unit area (counts per image); (e) Rose diagrams of the in-plane orientation distribution of grain lattice plane normals (relative to the horizontal direction). The data in (b-e) were obtained from statistical analysis of at least eight TEM images per condition; error bars represent the standard deviation.

The microstructure of MOP5M validates the strong confinement effect of the quasi-closed network chamber template. The crystallized area fraction is 12%, slightly lower than that of MO (13%) and comparable to MOP35k (11%), while the mean grain diameter is 2.8 nm, falling between MO (2.7 nm) and MOP35k (2.3 nm). Notably, the grain size distribution exhibits the narrowest spread among all systems, indicating exceptionally uniform grain dimensions. The orientation distribution, where measurable, shows no distinct preferred orientation (Figure 4e), consistent with the isotropic confinement of the quasi- closed network chambers that restricts grain growth equally in all directions and thus suppresses extensive grain development. These results above align with the continuously enhanced confinement indicated by UV-vis absorbance increase: pervasive network chambers partition precursors within micro-spaces, strongly inhibiting crystal nuclei development and promoting a predominantly amorphous structure with highly uniform grain characteristics.

In summary, TEM characterization directly visualizes the solid-state products guided by different degrees of template openness, forming a coherent evidentiary chain with solution behaviors revealed by MD simulations and UV-vis spectroscopy, providing a structural basis for understanding subsequent electrical performance differentiation.

3.4 Template Topology and Carrier Transport

To evaluate the influence of PEG molecular weight and concentration on the electrical properties of indium oxide semiconductor thin films, we performed comprehensive characterization of pure MO and MOP4k, MOP35k, MOP100k, and MOP5M devices (see Figure S7 for output characteristics and Figure 5a for transfer characteristics), extracting field-effect mobility (μ, Figure 5b), subthreshold swing (SS, Figure 5c), threshold voltage (V_{th}, Table 1), and on/off current ratio (I_{on}/I_{off}, Table 1). The concentration-dependent trends exhibit rigorous correspondence with the microstructural features, revealing how polymer templates achieve performance differentiation through modulation of the grain-amorphous composite structure. Pure MO exhibits a mobility of 0.89 cm^2/Vs, SS of 2.62 V/dec, V_{th} of -4.9 V, and on/off ratio of ~10^6, serving as a baseline for transport in the absence of template guidance.

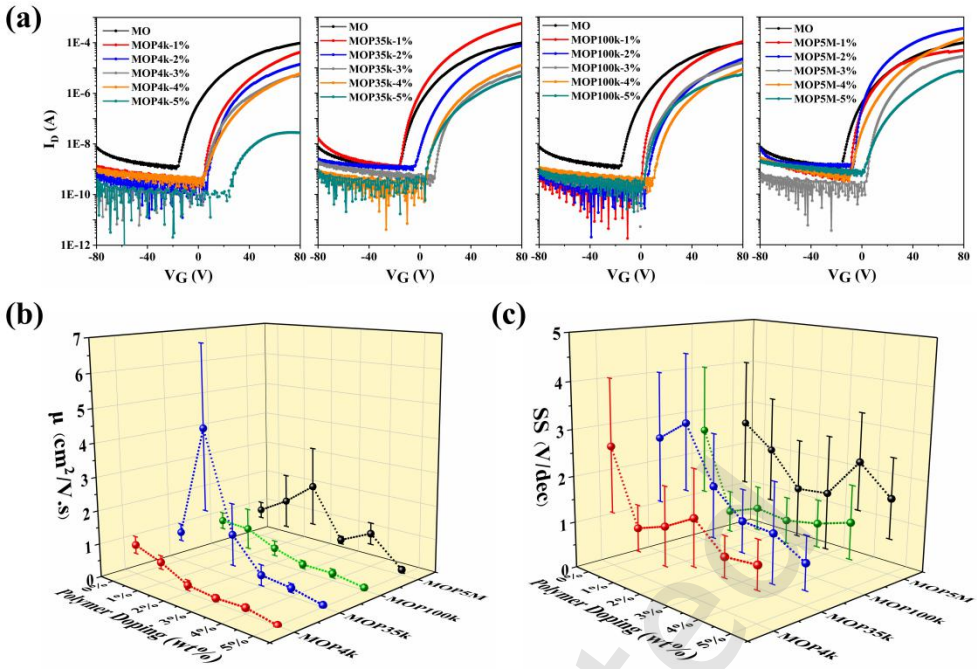

Figure 5 Electrical characteristics of pristine InO_x and polymer-blended TFTs with different PEG molecular weights and concentrations. (a) Transfer characteristics (I_D-V_{GS}) of TFTs based on MOP4k, MOP35k, MOP100k and MOP5M films measured at V_{DS}=30 V. (b) Three-dimensional plot of the field-effect mobility as a function of PEG molecular weight and concentration (including 0 wt% for pristine InO_x). (c) Corresponding three-dimensional plot of the SS. The data points represent average values extracted from at least 15 devices per condition; error bars represent the standard deviation.

MOP4k mobility decreases continuously and dramatically with increasing PEG concentration, dropping to 0.013 cm^2/Vs at 5%, with only a slight recovery at 4%. This monotonic deterioration correlates with the fully open point-like obstacle template—large disordered grains and narrow tortuous intergranular regions revealed by TEM form a high-scattering, high-trap transport network. SS improves initially at low concentrations, suggesting short-chain passivation of interface defects, followed by fluctuations with increasing concentration, reflecting exacerbated intergranular disorder. V_{th} exhibits a continuous, substantial positive shift (from -4.9 V to +19.6 V), indicating high-density electron trap accumulation, Fermi level pinning, and reduced effective carrier concentration consistent with mobility collapse. On/off ratio remains at 10^6–10^7, indicating retained gate control despite severely compromised transport efficiency.

MOP35k devices exhibit a sharp mobility peak at 1% concentration, reaching 4.28 cm^2/Vs—nearly five times that of pure MO—demonstrating the semi-open grid template's capability to construct efficient transport pathways through fine grains and high-quality amorphous matrix. However, this peak is accompanied by relatively high SS (3.08 V/dec) and pronounced negative V_{th} shift (-9.3 V), indicating that the optimal configuration for maximizing mobility does not simultaneously optimize switching characteristics and threshold control. The elevated SS may arise from both interfacial disorder induced by high-density nucleation and ionized impurity scattering from the high concentration of shallow donors, while the substantial negative V_{th} reflects increased carrier concentration that shifts operating voltage away from ideal near-zero values. Beyond 1%, mobility rapidly decays, SS continuously improves to 0.87 V/dec at 5%, and V_{th} shifts positively, indicating that the grid template maintains low interface state density even after deviating from the optimal window, possibly due to homogenization effects at high concentrations. On/off ratio remains stable at 10^6–10^7.

Table.1 I_{on}/I_{off} ratio and threshold voltage of InO_x/PEG-TFTs

Sample	I_{on}/I_{off}	Threshold voltage (V)
0	~10^6	-4.9
MOP4k-1%	~10^7	6.7
MOP4k-2%	~10^7	10.1
MOP4k-3%	~10^7	9.9
MOP4k-4%	~10^7	15.3
MOP4k-5%	~10^6	19.6
MOP35k-1%	~10^7	-9.3
MOP35k-2%	~10^6	3.1
MOP35k-3%	~10^7	12.6
MOP35k-4%	~10^7	10.7
MOP35k-5%	~10^6	26
MOP100k-1%	~10^7	4.9
MOP100k-2%	~10^8	11.6
MOP100k-3%	~10^6	11.8
MOP100k-4%	~10^7	14.5
MOP100k-5%	~10^6	10.6
MOP5M-1%	~10^8	-3.9
MOP5M-2%	~10^7	-1.4
MOP5M-3%	~10^7	2.6
MOP5M-4%	~10^6	0.11
MOP5M-5%	~10^6	10.8

MOP100k devices fail to exceed the pure MO baseline across all concentrations, with mobility remaining between 0.85 cm^2/Vs and 0.08 cm^2/Vs. This mediocre performance aligns with the uniaxially open continuous template—relatively large grains and concentrated orientation provide local ordering, but intergranular amorphous matrix suffers from uneven quality due to template rigidity and spatial asymmetry, forming discontinuous transport bottlenecks. SS improves significantly at 1% (0.88 V/dec), indicating effective interface defect passivation at low concentrations, but gradually increases with further addition, reflecting interface quality deterioration. V_{th} shifts positively even at 1%, reaching 14.5 V at higher concentrations, suggesting carrier capture by numerous interface/bulk traps. On/off ratio reaches 10^8 at 1%, indicating excellent off-current control, but mediocre mobility renders this advantage practically insignificant.

MOP5M devices exhibit the most balanced overall performance. Mobility displays a broad-concentration

optimization, peaking at 2.08 cm^2/Vs at 2% and remaining above pure MO across the 1–4% range, demonstrating robust enhancement with exceptional process tolerance. Critically, this mobility enhancement is accompanied by well-behaved switching characteristics: SS continuously improves from 2.11 V/dec at 1% to 1.35 V/dec at 2%, significantly outperforming pure MO and indicating effective reduction of interface trap density. Furthermore, V_{th} evolution is the most moderate among all systems, with values remaining near zero at optimal concentrations (0.11 V at 4%), demonstrating near-ideal threshold control. This balanced combination—enhanced mobility, reduced SS, and well-controlled V_{th}, maintained over a broad concentration window—aligns with the strong physical confinement of the quasi-closed network chamber template, which suppresses excessive crystalline growth and guides formation of a uniform, dense amorphous-dominated structure with well-controlled grain distribution. On/off ratio remains stable at 10^6-10^8.

A noteworthy cross-system phenomenon is that near 3-4 wt% concentration, the declining mobility trend for all systems tends to slow or exhibit slight recovery, suggesting that at relatively high concentrations, physical filling and continuous phase formation begin to emerge, partially modulating the extreme structural differentiation dominated by template morphology.

In summary, systematic electrical measurements provide strong validation for the template openness mechanistic model. MOP4k leads to continuous performance deterioration across all metrics. MOP100k fails to achieve effective enhancement despite some SS improvement at low concentrations. Notably, MOP35k and MOP5M demonstrate two fundamentally different yet successful performance regulation paradigms. MOP35k achieves exceptional mobility enhancement through its semi-open grid template, but this comes at the cost of degraded SS and V_{th} control at the optimal concentration, with enhancement confined to an extremely narrow processing window. In contrast, MOP5M delivers more balanced overall performance—respectable mobility enhancement, significantly improved SS, and near-ideal V_{th} control—maintained over a broad concentration range, offering superior process tolerance and more predictable device characteristics. These macroscopic electrical trends exhibit good correspondence with microstructural features and provide clear guidance for selecting appropriate polymer additives based on specific application requirements.

3.5 Defect Chemistry and Performance Origin

To elucidate the chemical origins of the observed differences in electrical performance, X-ray photoelectron spectroscopy was performed on films from each system, deconvoluting the O 1s spectra into three components: lattice oxygen (O_A, ~530.0 eV), oxygen vacancy-related oxygen (O_B, ~531 eV), and adsorbed/defective oxygen (O_C, ~532.0 eV), which were shown in Figure S8[31-33], and area ratios of O_A, O_B and O_C were shown in Table 2. With a film thickness of approximately 5 nm, well below the XPS information depth, the acquired data faithfully represent the bulk chemical state. The evolution of each component with molecular weight and concentration (shown in Figure 6) exhibits direct correspondence with the microstructural and electrical characteristics discussed above.

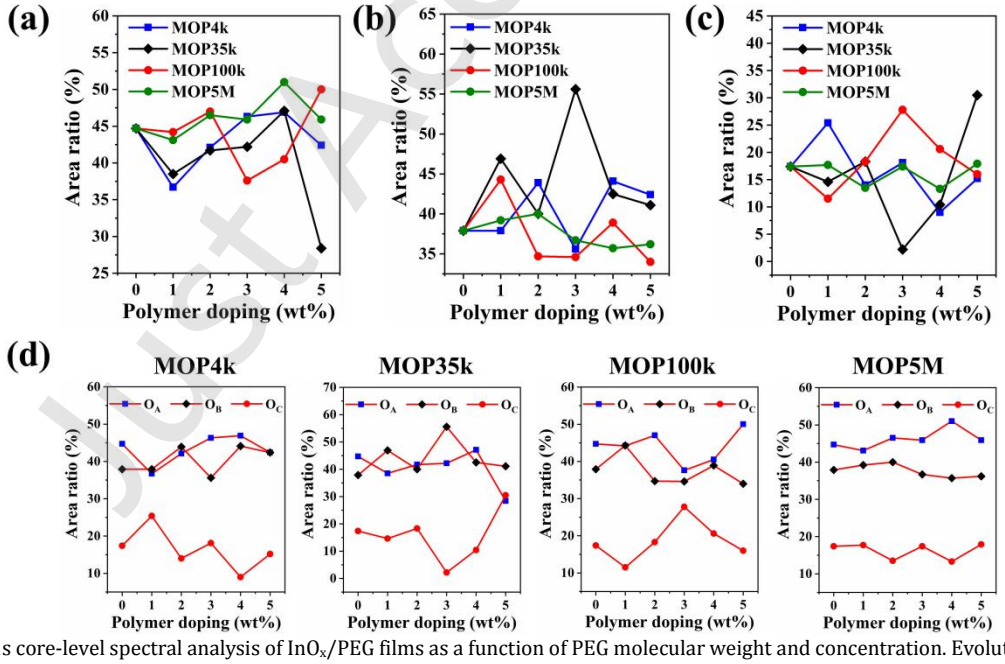

Figure 6 XPS O 1s core-level spectral analysis of InO_x/PEG films as a function of PEG molecular weight and concentration. Evolution of the area fractions of (a) lattice oxygen (O_A), (b) oxygen vacancy-related oxygen (O_B) and (c) adsorbed/defective oxygen (O_C) with increasing PEG concentration for MOP4k, MOP35k, MOP100k and MOP5M. (d) Detailed variation of the three oxygen species (O_A, O_B, O_C) for each individual polymer system plotted together in a single panel to reveal intra-system compositional trends.

MOP4k films exhibit an anomalously high O_C fraction. At 1% concentration, O_C reaches 25.4%, far exceeding the 17.4% of pure MO, with O_A decreasing to 36.7%. As concentration increases, O_C fluctuates dramatically, while O_A and O_B exhibit no stable trend. This indicates that the continuously dispersed obstacle field template severely disrupts precursor condensation, resulting in films populated with deep-level trap states. These O_C species form deep trap levels that efficiently capture free electrons, drastically reducing effective carrier concentration while exacerbating scattering—providing the chemical basis for continuous mobility deterioration and the substantial positive V_{th} shift (up to +19.6 V).

MOP35k films at 1% concentration exhibit a distinctive high O_B, low O_C signature: O_B surges to 46.9%, O_C decreases to 14.6%. This represents direct evidence of precise defect

chemistry modulation by the semi-open grid template, which provides a perturbation-free condensation environment, homogeneously introducing high concentrations of shallow-donor oxygen vacancies while suppressing deep-level defects. This chemical state explains the extreme electrical performance: high O_B supplies abundant free electrons (manifested as the pronounced negative V_{th} shift to -9.3 V), while low O_C ensures carriers remain free from deep trap scattering, simultaneously enabling high mobility (4.28 cm^2/Vs) and good gate control. However, this optimized state is extremely sensitive to concentration. At 2%, O_B decreases to 40.0% and O_C increases to 18.3%. At 3%, O_B anomalously reaches 55.6% with O_C at 2.2%, possibly corresponding to a highly defective but cleaned state. By 5%, O_C rebounds to 30.5%, marking complete loss of the optimization mechanism. This sensitive evolution mirrors the sharp peak in electrical performance.

MOP100k films exhibit pronounced concentration threshold effects and incoherence in chemical state evolution. At 1%, O_B is 44.3%, O_C is 11.5%, superficially resembling the MOP35k-1% composition. Although both MOP100k and MOP4k have large grains and high crystallinity, MOP100k exhibits higher O_B and lower O_C than MOP4k, possibly due to its uniaxial grain orientation that yields more ordered grain boundaries with fewer dangling bonds. However, the underlying microstructure prevents these locally beneficial defects from being embedded within a globally low-trap network, resulting in mediocre mobility (0.85 cm^2/Vs). As concentration increases, the chemical state fluctuates widely, with O_B ranging from 34.7-44.3%, O_C from 11.5-27.8%, and O_A from 37.6-47.0%, reflecting the single continuous obstacle field template's inherent incapability of precisely modulating defect distribution. This unpredictable volatility constitutes the fundamental origin of its mediocre and unstable electrical performance.

Table.2 Area ratio of O_A, O_B and O_C

Sample	O_A	O_B	O_C
0	44.70%	37.90%	17.40%
MOP4k-1%	36.70%	37.90%	25.40%
MOP4k-2%	42.10%	43.90%	14.00%
MOP4k-3%	46.30%	35.60%	18.10%
MOP4k-4%	46.90%	44.10%	9.00%
MOP4k-5%	42.40%	42.40%	15.20%
MOP35k-1%	38.50%	46.90%	14.60%
MOP35k-2%	41.70%	40.00%	18.30%
MOP35k-3%	42.20%	55.60%	2.20%
MOP35k-4%	47.10%	42.50%	10.40%
MOP35k-5%	28.40%	41.10%	30.50%
MOP100k-1%	44.20%	44.30%	11.50%
MOP100k-2%	47.00%	34.70%	18.30%
MOP100k-3%	37.60%	34.60%	27.80%
MOP100k-4%	40.50%	38.90%	20.60%
MOP100k-5%	50.00%	34.00%	16.00%
MOP5M-1%	43.10%	39.20%	17.70%
MOP5M-2%	46.50%	40.00%	13.50%
MOP5M-3%	45.90%	36.70%	17.40%
MOP5M-4%	51.00%	35.70%	13.30%
MOP5M-5%	45.90%	36.20%	17.90%

MOP5M films exhibit the most stable chemical state evolution. Across the entire 1-5% concentration range, O_B remains within 35.7-40.0%, O_C is consistently low at 13.3-17.9%, and O_A fluctuates narrowly between 43.1-51.0%. This demonstrates that the quasi-closed network chamber template imposes uniform physicochemical constraints, gently enhancing beneficial oxygen vacancy concentrations while universally suppressing deep-level defects. This stability corresponds perfectly with electrical performance that robustly exceeds pure MO across a broad concentration window (1-4%). The moderate O_B provides stable carrier increments (reflected in mild V_{th} shifts), while consistently low O_C ensures minimal trap scattering, yielding a peak mobility of 2.08 cm^2/Vs at 2% with continuously improving SS.

Notably, near 3-4% concentration, all systems exhibit a universal increase in O_A fraction. This correlates with the stabilization or slight recovery in electrical performance, suggesting that at sufficiently high polymer concentration, the continuous phase induces a structural homogenization effect, partially repairing extreme chemical states.

In summary, XPS analysis anchors the observed electrical differences to defect chemistry. MOP4k suffers performance collapse due to deep trap (high O_C) enrichment. MOP35k achieves a golden balance of shallow donor (high O_B) enrichment and deep trap suppression at optimal concentration, pushing the performance limit within a narrow processing window. MOP100k, constrained by a template structure incapable of precise defect modulation, exhibits unpredictable chemical state evolution and consequently mediocre, unstable performance. MOP5M, through uniform and robust defect engineering, achieves broad-window performance enhancement with superior process tolerance. This chemical state landscape provides direct electronic structure evidence for the polymer template strategy.

3.6 Programming the Band Landscape via Template Openness

Integrating multi-scale characterization results, we establish a structure-property relationship elucidating how PEG molecular weight, through defining template openness, synergistically programs carrier transport in indium oxide films from microstructural and defect chemistry perspectives, as illustrated schematically in Figure 7. Template openness determines the geometric characteristics of the nanocrystalline-amorphous composite and the chemical state of the amorphous matrix, thereby shaping the band landscape and pathway efficiency for carrier transport.

① MOP4k (fully open point-like template). Large disordered grains are embedded in a defective amorphous matrix, with direct grain-grain contact forming high-energy grain boundaries. The amorphous matrix and grain boundary regions are rich in deep traps. In the band diagram, these deep traps cause Fermi level pinning deep in the bandgap, while the grain boundaries create sharp potential barriers. Consequently, carriers are trapped in an inefficient drift–capture–release cycle, leading to substantial positive V_{th} shifts and severely degraded mobility.

② MOP35k (semi-open grid template). Fine uniform grains are embedded in a high-quality amorphous matrix, separated by thin, high-quality amorphous layers without direct grain-grain contact. The amorphous matrix is uniformly enriched with shallow donors. In the band diagram, shallow donors near the conduction band minimum provide abundant free electrons with minimal scattering, while the absence of grain-boundary barriers results in a smooth band landscape. Carriers transport efficiently through the percolation network formed by grains and the shallow donor-enriched amorphous matrix, elevating mobility to 4.28 cm^2/Vs. The high shallow donor concentration shifts the Fermi level upward, manifesting as a pronounced negative V_{th} shift, though this optimized state is confined to a narrow concentration window.

③ MOP100k (uniaxially open continuous

template). Oriented large grains are embedded in amorphous matrix. Direct grain-grain contact occurs in certain regions, creating high-energy grain boundaries and sharp potential barriers in the band diagram. Unlike MOP4k, however, the amorphous matrix contains more shallow donors and fewer deep traps. Despite this favorable defect chemistry, the sharp grain-boundary barriers dominate transport, resulting in intermittently connected pathways and consistently mediocre mobility.

④ MOP5M (quasi-closed network chamber template). The film is dominated by a uniform dense amorphous matrix with a small fraction of well-dispersed fine grains. Shallow donors are uniformly distributed throughout the matrix, while deep traps are minimal. In the band diagram, the absence of grain boundaries yields a smooth band landscape with low defect state density. Carrier transport relies primarily on extended state transport or thermally assisted hopping through band tail states, yielding continuous pathways. While peak mobility (2.08 cm^2/Vs) is lower than that of MOP35k, it robustly exceeds the baseline across a broad concentration window, with smooth V_{th} evolution and continuously improving SS.

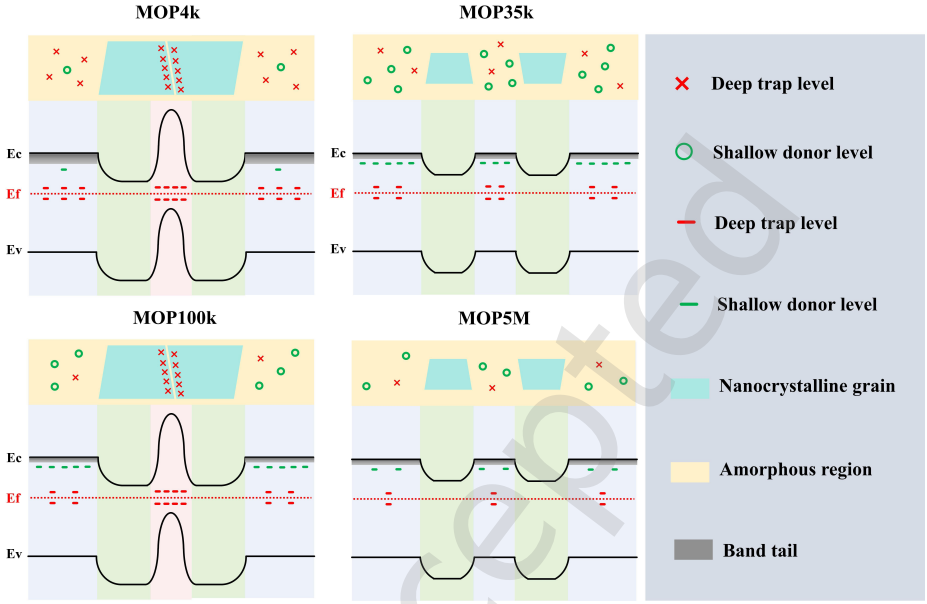

Figure 7 Schematic illustration of the structure-property relationship in InO_x/PEG composite films as a function of PEG molecular weight.

Synthesizing these scenarios within the unified template openness framework reveals a clear hierarchy in band landscape engineering. Open templates, whether fully open or uniaxially open, are uniformly characterized by sharp grain-boundary barriers that dominate carrier transport, rendering even favorable defect chemistry insufficient for efficient conduction. In contrast, the semi-open grid and quasi-closed network templates both achieve barrier-free transport pathways, yet through distinct mechanisms. The former constructs percolation networks via structural ordering and shallow donor enrichment, enabling peak performance at the cost of a narrow processing window. The latter achieves transport through structural homogeneity and stable defect chemistry, delivering robust performance across a broad concentration range. Thus, template openness establishes a direct link from chain-level spatial organization to device-level transport behavior, demonstrating that polymer molecular weight serves not merely as a processing parameter but as a topological design handle for programming the coupled microstructure-defect landscape. The identification of two orthogonal yet equally effective paradigms provides a versatile platform for decoupling and independently optimizing the key determinants of carrier transport: grain size, grain boundaries, amorphous matrix quality, and defect chemistry. Architecture-driven percolation prioritizes extreme peak performance, while confinement-driven homogenization favors robust process tolerance and near-ideal threshold. This framework offers a rational design blueprint for printed oxide electronics, where material performance can be tailored to specific application needs simply by selecting the appropriate template openness.

4 Conclusions

This study reveals that PEG molecular weight programs the spatial distribution of chain segments in solution, defining a continuous template spectrum from fully open to quasi-closed that governs nucleation and growth kinetics, enabling synergistic modulation of microstructure, defect chemistry, and electrical performance. The semi-open grid template of MOP35k-1% achieves exceptional mobility (4.28 cm^2 /Vs) through fine nanocrystals embedded in a high-quality amorphous matrix with high-O_B/low-O_C defect chemistry, albeit confined to a narrow processing window with non-ideal threshold. The quasi-closed network template of MOP5M similarly achieves nanocrystalline–amorphous synergy, with comparable crystallinity and exceptionally uniform grain size distribution, delivering robust performance across a broad concentration range. In contrast, both the fully open template (MOP4k) and the uniaxially open template (MOP100k) suffer from large grains that form high-energy grain boundaries, creating sharp potential barriers that dominate transport; the latter additionally induces grain orientation but fails to overcome this barrier-dominated bottleneck.

This work elevates polymer molecular weight from a conventional processing additive to a spatial template design parameter, establishing template openness as a unifying framework that links chain organization, film microstructure, defect chemistry, and device performance. The identification of two orthogonal yet equally effective paradigms provides a versatile molecular engineering toolkit for printed oxide electronics. Architecture-driven percolation prioritizes extreme peak performance, while confinement-driven

homogenization delivers robust process tolerance with near-ideal threshold. These findings offer design guidelines for selecting polymer additives according to specific application requirements. As a step toward a more quantitative description, future work could define a semi-quantitative openness index, for example based on the number of effective confinement directions or the free volume fraction estimated from MD simulations. Nevertheless, while the "template openness" framework may be extendable to other oxide/polymer systems, its application to polymers with strong coordinating groups would likely involve additional complexity due to the interplay between physical confinement and chemical coordination, warranting further investigation.

Electronic Supplementary Material: Supplementary material (please provide the brief detail of the ESM) is available in the online version of this article at https://doi.org/10.26599/NR.2026.94908837.

Data availability

All data needed to support the conclusions in the paper are presented in the manuscript and/or the Electronic Supplementary Material. Additional data related to this paper may be requested from the corresponding author upon request.

Acknowledgements

This work is granted by National Natural Science Foundation of China (62504042), Basic and Applied Basic Research Foundation of Guangdong Province (2023A1515110284) and The Open Fund of the Guangdong Provincial Key Laboratory of Fiber Laser Materials and Applied Techniques (2025-09).

Declaration of competing interest

All the contributing authors report no conflict of interests in this work.

Author contribution statement

Z.N.Z: Conceptualization, Data curation, Formal analysis, Funding acquisition, Investigation, Methodology, Project administration, Supervision, Writing-original draft, Writing-review & editing.
W.L: Methodology, Resources, Supervision.
X.J.K: Methodology, Resources, Supervision.
J.L.S: Data curation, Investigation.
X.M.C: Data curation, Investigation.
Q.W.P: Funding acquisition, Methodology.
R.H.Y: Methodology, Resources.
H.C.W: Project administration, Resources, Supervision.
H.L.N: Conceptualization, Project administration, Supervision, Writing - review & editing.
All the authors have approved the final manuscript.

Informed consent

Not applicable.

Ethics statement

Not applicable.

Use of AI statement

During the preparation of this work, the authors used DeepSeek in order to improve readability and language of some parts of this paper. After using this tool, the authors reviewed and edited the content as needed and take full responsibility for the content of the publication.

References

[1] Ren, S.; Huang, Q.; Li, D.; Wang, S.; Chen, Y.; Ren, H.; Wang, Y.; Tang, Y.; Zhu, B. Oxide semiconductor thin‐Film transistors for low‐power electronics. *Adv. Sci.* **2026**, *13*, e22487.

[2] Yu, S.; Deng, W.; Wu, X.; Ren, Y.; Xie, Y.; Sun, S.; Sun, L.; Yang, F.; Zhang, H.; Hu, W. Fully printed organic thin-film transistors: pathways to scalable, high-performance flexible electronics. *Chem. Soc. Rev.* **2026**, *55*, 567-604.

[3] Huang, L.; Zhao, D.; Yan, X.; Liu, X.; Sun, Q.; Yang, H.; Liu, X.; Jia, H. Organic electrochemical transistors: from lithography to large‐scale printing. *Adv. Electron. Mater.* **2025**, *11*, 2400474.

[4] Cantarella, G.; Costa, J.; Meister, T.; Ishida, K.; Carta, C.; Ellinger, F.; Lugli, P.; Münzenrieder, N.; Petti, L. Review of recent trends in flexible metal oxide thin-film transistors for analog applications. *Flex. Print. Electron.* **2020**, *5*, 33001.

[5] Jeon, S.; Jo, J.; Nam, D.; Kim, Y.; Park, S. K. High-performance metal oxide TFTs for flexible displays: materials, fabrication, architecture, and applications. *Soft Sci.* **2025**, *5*, 1.

[6] Geng, D.; Wang, K.; Li, L.; Myny, K.; Nathan, A.; Jang, J.; Kuo, Y.; Liu, M. Thin-film transistors for large-area electronics. *Nat. Electron.* **2023**, *6*, 963-972.

[7] Nguyen, Q. K.; Pham, G. H.; Chu, T. T. H.; Tran, D. C.; Yu, S. H.; Cho, S.; Sung, M. M. Phase-composite InO_x semiconductors for high-performance flexible thin-film transistors. *ACS Appl. Mater. Interfaces* **2025**, *17*, 22912-22920.

[8] Kim, J.; Lee, S.; Cho, W.; Park, H. Tailoring electrical stability of indium oxide thin-film transistors via solution aging-induced defect modulation. *ACS Appl. Electron. Mater.* **2025**, *7*, 6187-6195.

[9] Tao, Z.; Zheng, P.; Dong, G.; Liu, M. The mechanical behaviors in oxides: beyond brittleness. *Adv. Mater.* **2026**, e15834.

[10] Hamlin, A. B.; Ye, Y.; Huddy, J. E.; Rahman, M. S.; Scheideler, W. J. 2D transistors rapidly printed from the crystalline oxide skin of molten indium. *Npj 2D Mater. Appl.* **2022**, *6*, 16.

[11] Lee, S. J.; Ko, J.; Nam, K.; Kim, T.; Lee, S. H.; Kim, J. H.; Chae, G. S.; Han, H.; Kim, Y. S.; Myoung, J. Fully solution-processed and foldable metal-oxide thin-film transistor. *ACS Appl. Mater. Interfaces* **2016**, *8*, 12894-12900.

[12] Divya, M.; Cherukupally, N.; Gogoi, S. K.; Pradhan, J. R.; Mondal, S. K.; Jain, M.; Senyshyn, A.; Dasgupta, S. Super flexible and high mobility inorganic/organic composite semiconductors for printed electronics on polymer substrates. *Adv. Mater. Technol.* **2023**, *8*, 2300256.

[13] Yu, X. G.; Zeng, L.; Zhou, N. J.; Guo, P. J.; Shi, F. Y.; Buchholz, D. B.; Ma, Q.; Yu, J. S.; Dravid, V. P.; Chang, R.et al. Ultra-flexible, "invisible" thin-film transistors enabled by amorphous metal oxide/polymer channel layer blends. *Adv. Mater.* **2015**, *27*, 2390-2399.

[14] Kwak, T.; Yang, H.; Chung, J.; Kim, M.; Jung, S.; Park, G.; Kim, F. S. Polymer-induced surface wrinkling and imine polymer-based doping of sol–gel zinc oxide in electrolyte-gated transistors. *Macromol. Res.* **2025**, *33*, 49-55.

[15] Huang, W.; Guo, P. J.; Zeng, L.; Li, R.; Wang, B. H.; Wang, G.; Zhang, X. A.; Chang, R.; Yu, J. S.; Bedzyk, M. J.et al. Metal composition and polyethylenimine doping capacity effects on semiconducting metal oxide-polymer blend charge transport. *J. Am. Chem. Soc.* **2018**, *140*, 5457-5473.

[16] Wang, Z.; Zhuang, X.; Wang, B.; Huang, W.; Marks, T. J.; Facchetti, A. Doping indium oxide films with amino‐polymers of varying

nitrogen content markedly affects charge transport and mechanical flexibility. *Adv. Funct. Mater.* **2021**, *31*, 2100451.

[17] Lee, E. G.; Gong, Y. J.; Lee, S. E.; Na, H. J.; Im, C.; Kim, H.; Kim, Y. S. Conductive polymer-assisted metal oxide hybrid semiconductors for high-performance thin-film transistors. *ACS Appl. Mater. Interfaces* **2021**, *13*, 8552-8562.

[18] Huang, W.; Chien, P. H.; McMillen, K.; Patel, S.; Tedesco, J.; Zeng, L.; Mukherjee, S.; Wang, B. H.; Chen, Y.; Wang, G.et al. Experimental and theoretical evidence for hydrogen doping in polymer solution-processed indium gallium oxide. *Proc. Natl. Acad. Sci. U. S. A.* **2020**, *117*, 18231-18239.

[19] Song, G.; Zhang, X.; Xu, H. Carrier modulation and effective passivation of tin oxide thin-film transistors by organic surface doping. *Solid-State Electron.* **2024**, *221-222*, 109005.

[20] Zhu, Z.; Lv, W.; Wang, H.; Kang, X.; Pan, Q.; Yao, R.; Ning, H. Chain-length-dependent nanostructure evolution in InO_x/PAM composite films: Interface engineering for electrical performance modulation. *Surf. Interfaces* **2025**, *72*, 107039.

[21] Deepa, M.; Kar, M.; Singh, D. P.; Srivastava, A. K.; Ahmad, S. Influence of polyethylene glycol template on microstructure and electrochromic properties of tungsten oxide. *Sol. Energy Mater. Sol. Cells* **2008**, *92*, 170-178.

[22] Shi, X.; Pan, L.; Chen, S.; Xiao, Y.; Liu, Q.; Yuan, L.; Sun, J.; Cai, L. Zn(II)-PEG 300 globules as soft template for the synthesis of hexagonal ZnO micronuts by the hydrothermal reaction method. *Langmuir* **2009**, *25*, 5940-5948.

[23] Sørensen, I. E.; Thormann, E. Quantifying hofmeister effects on polymer-water interactions through freezing point depression. *Langmuir* **2026**, *42*, 6261-6267.

[24] Seward, T. M.; Henderson, C.; Charnock, J. M. Indium(III) chloride complexing and solvation in hydrothermal solutions to 350 ℃: an EXAFS study. *Chem. Geol.* **2000**, *167*, 117-127.

[25] Ohki, T.; Harada, M.; Okada, T. Structural and thermodynamic aspects of ionic solvation in concentrated aqueous poly (ethylene glycol). *J. Phys. Chem. B* **2007**, *111*, 7245-7252.

[26] Nazmutdinov, R. R.; Shapnik, M. S.; Malyucheva, O. I. Reduction pathways of indium ions: multistep discharge or disproportionation? *Russ. J. Electrochem.* **1993**, *29*, 428-433.

[27] Aparna, C.; Mahesha, M. G.; Shetty, P. K. Structural and optical properties of indium oxide thin films synthesized at different deposition parameters by spray pyrolysis. *Mater. Today: Proc.* **2022**, *55*, 141-147.

[28] Hyun, K.; Jin, H.; Woo, W. H.; Shin, H.; Lee, J. H.; Hwang, H.; Kim, M.; Lee, K. M.; Park, M. H.; Kim, Y. Systematic design of indium-based luminophores with color-tunable emission via combined manipulation of HOMO and LUMO levels. *Dyes Pigm.* **2018**, *158*, 285-294.

[29] Qu, C.; Lv, C.; Liu, J. Preparation and characterization of hollow spherical indium tin oxide with micro size by template assisted hydrothermal method. *J. Sol-Gel Sci. Technol.* **2024**, *111*, 38-48.

[30] DeLacy, B. G.; Lacey, S.; Zhang, D.; Valdes, E.; Hoang, K. Controlling the morphology of indium tin oxide using PEG-assisted hydrothermal synthesis. *Mater. Lett.* **2014**, *117*, 108-111.

[31] Blume, R.; Calvet, W.; Ghafari, A.; Mayer, T.; Knop Gericke, A.; Schlögl, R. Structural and chemical properties of NiO_x thin films: oxygen vacancy formation in O_2 atmosphere. *Chemphyschem* **2023**, *24*, e202300231.

[32] Andersson, T. G.; Andreasson, M.; Klement, U.; Lee, C. B.; Pujilaksono, B.; Uddin, A. Preparation and characterization of the ITO surface and the Al/Alq_3/ITO heterostructure for OLEDs. *Mater. Sci. Eng., B* **2007**, *145*, 48-56.

[33] Hewitt, R. W.; Winograd, N. Oxidation of polycrystalline indium studied by x‐ray photoelectron spectroscopy and static secondary ion mass spectroscopy. *J. Appl. Phys.* **1980**, *51*, 2620-2624.

Electronic Supplementary Material

Templating openness engineering: A strategy for performance enhancement via synergistic nanocrystalline-amorphous composite in solution-processed InO_x/PEG TFTs

Zhennan Zhu[1], Wei Lv[1], Xiaojiao Kang[1], Jialing Sun[1], Xuemei Chen[1], Qiwen Pan[1], Rihui Yao[2], Hongcheng Wang [1]✉, and Honglong Ning [2,3]✉

[1] *School of Electrical Engineering and Intelligentization, Dongguan University of Technology, Dongguan 523808, China*
[2] *Guangdong Basic Research Center of Excellence for Energy & Information Polymer Materials, State Key Laboratory of Luminescent Materials and Devices, School of Materials Sciences and Engineering, South China University of Technology, Guangzhou 510640, China*
[3] *The International School of Microelectronics, Dongguan University of Technology, Dongguan 523808, China.*

✉Address correspondence to Hongcheng Wang, wanghc@dgut.edu.cn; Honglong Ning, ninghl@scut.edu.cn

Supporting information to https://doi.org/10.26599/NR.2026.94908837

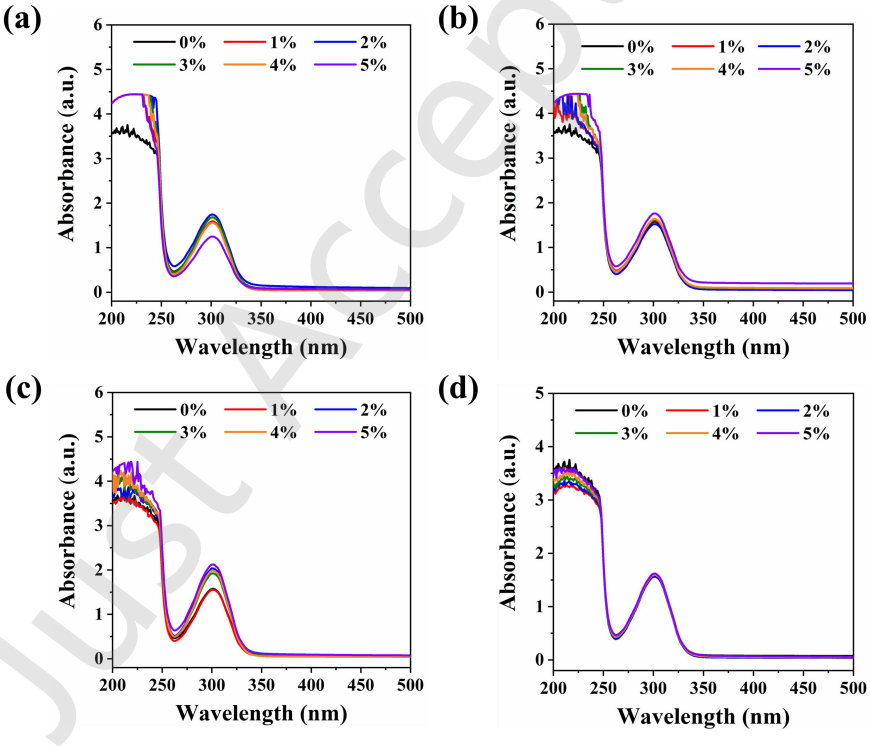

Figure S1 UV spectra of (a) MOP4k, (b) MOP35k, (c) MOP100k and (d) MOP5M at range of 200-500 nm.

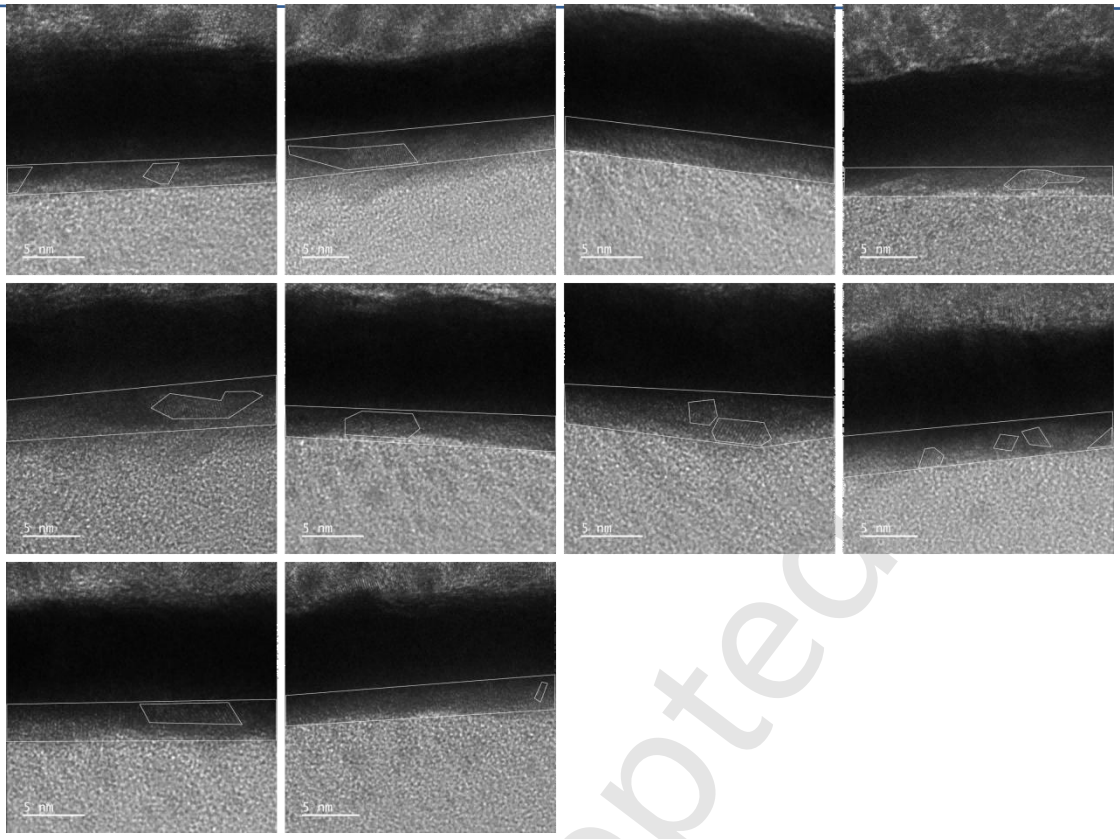

Figure S2 Representative FIB-TEM images of pristine InO_x (MO) with manually delineated grain boundaries (white outlines).

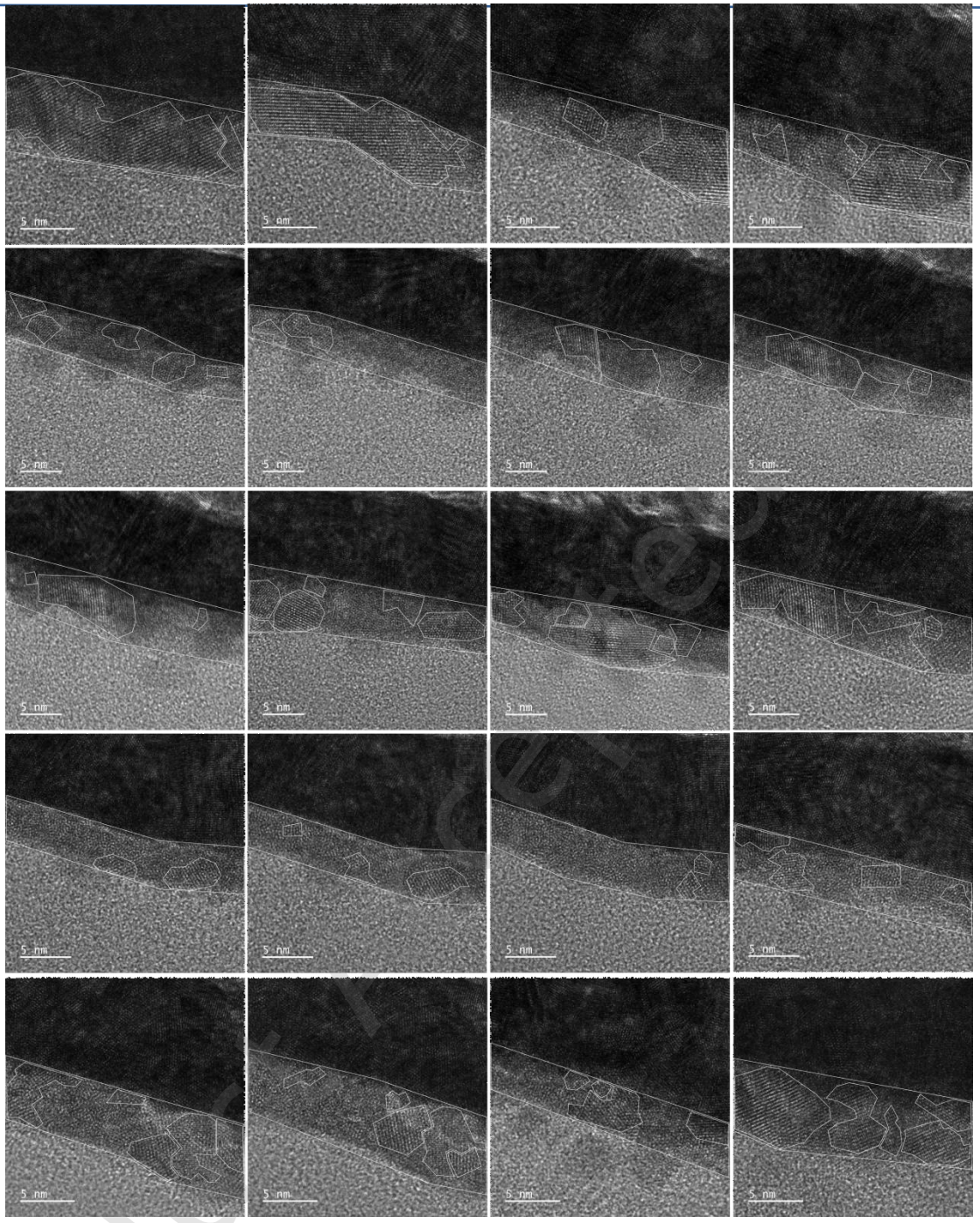

Figure S3 Representative FIB-TEM images of MOP4k-1% with manually delineated grain boundaries (white outlines).

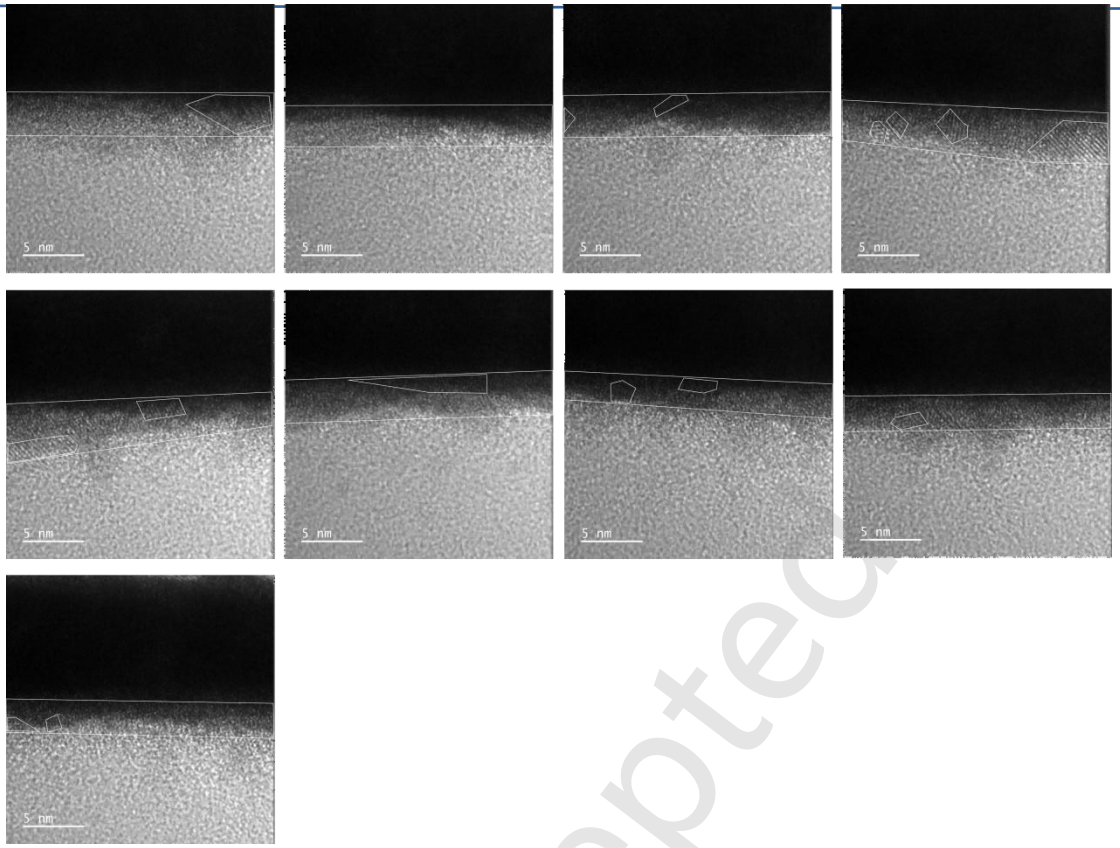

Figure S4 Representative FIB-TEM images of MOP35k-1% with manually delineated grain boundaries (white outlines).

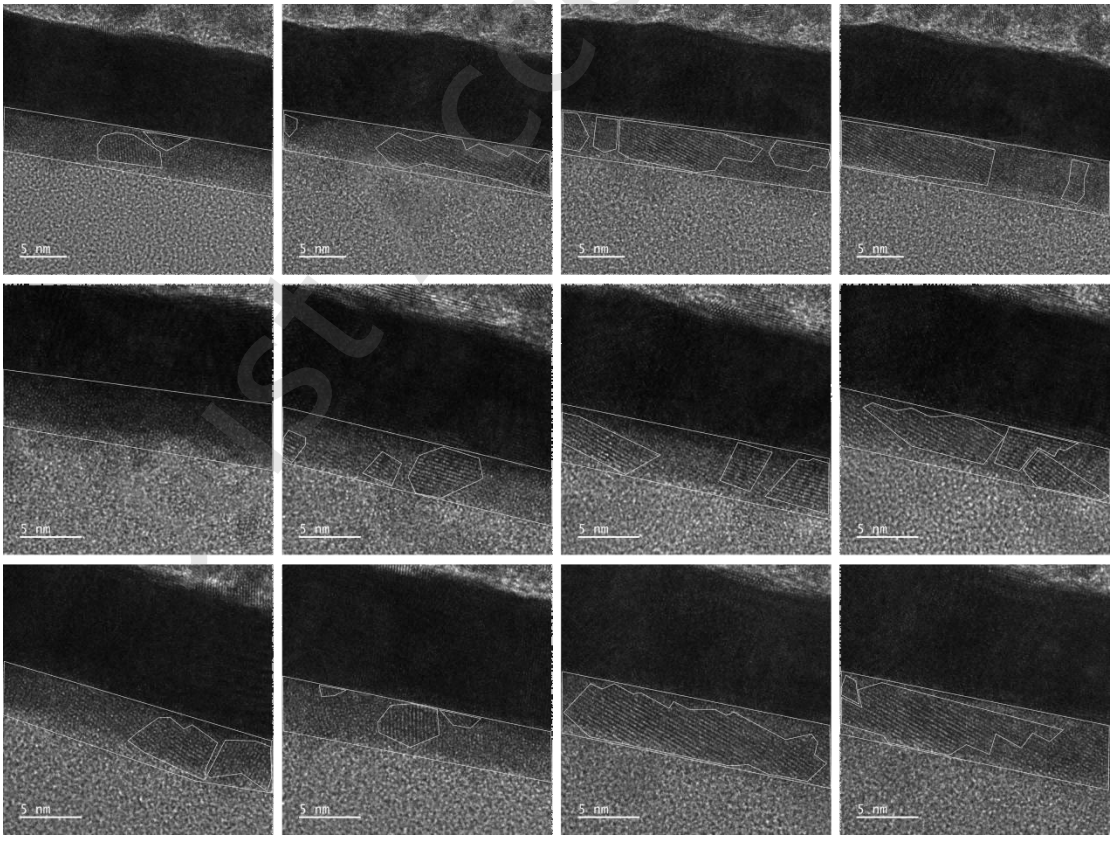

Figure S5 Representative FIB-TEM images of pristine MOP100k-1% with manually delineated grain boundaries (white outlines).

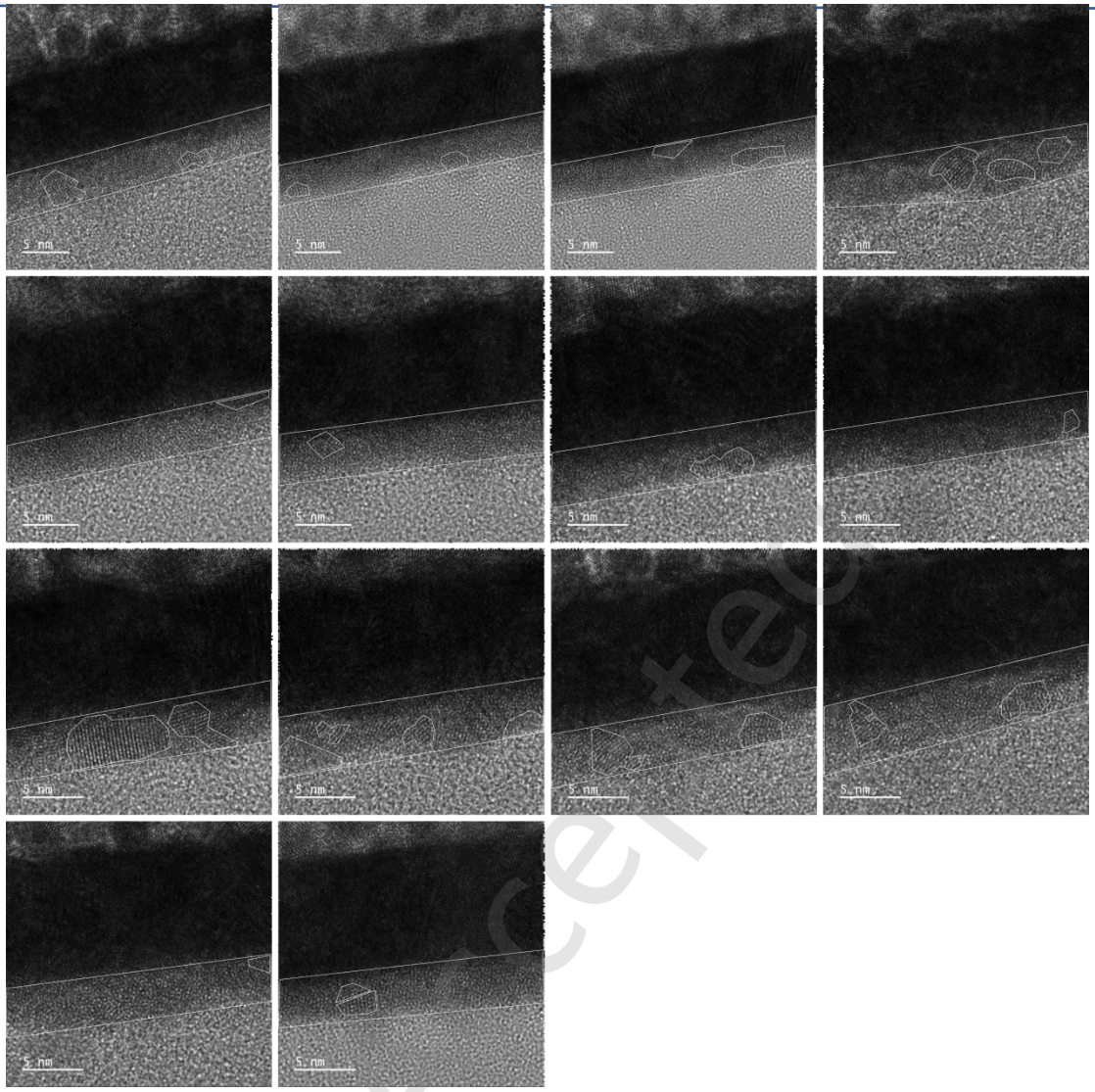

Figure S6 Representative FIB-TEM images of MOP5M-1% with manually delineated grain boundaries (white outlines).

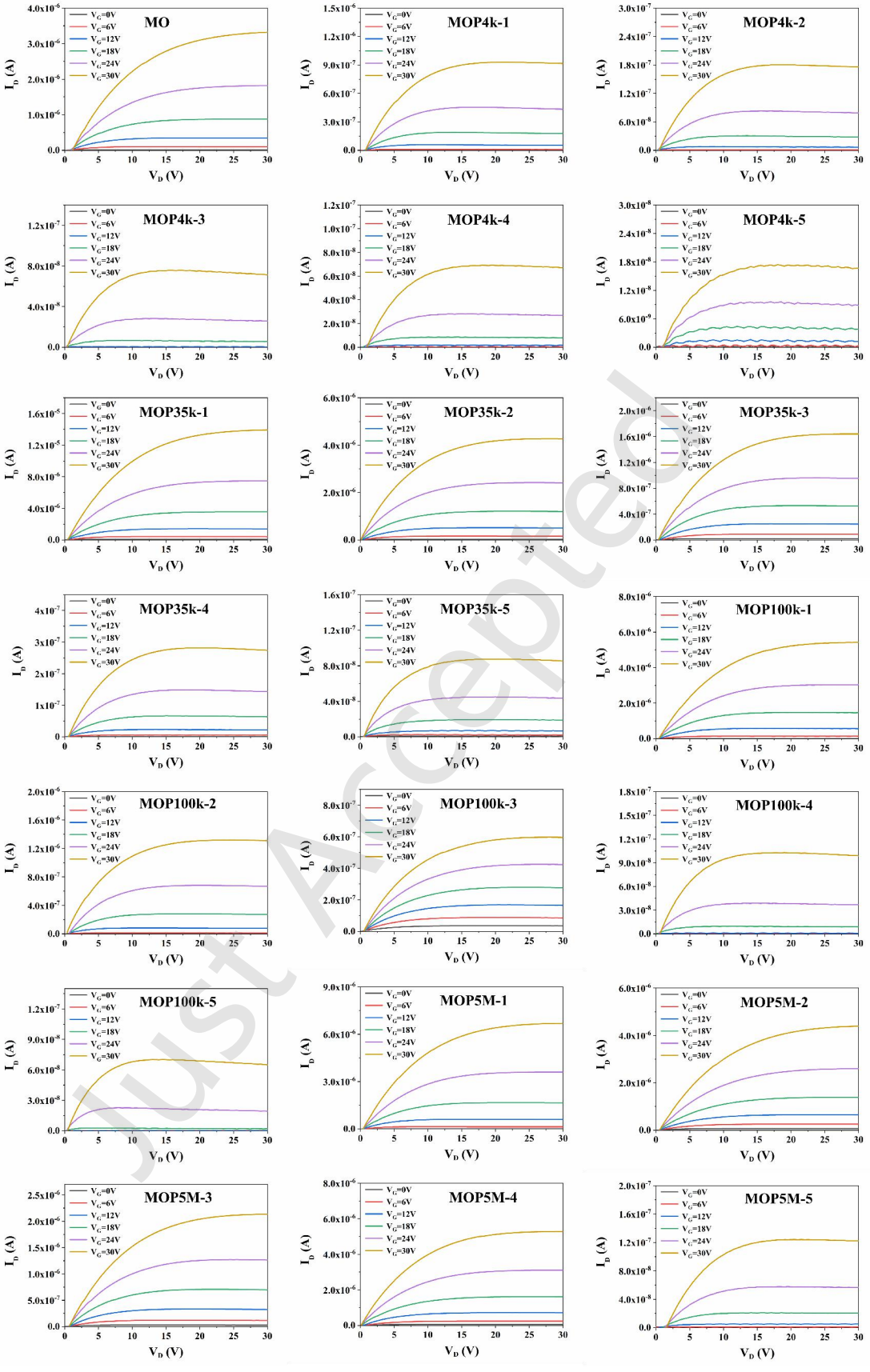

Figure S7 The output characteristic curves of InO_X/PEG-TFTs

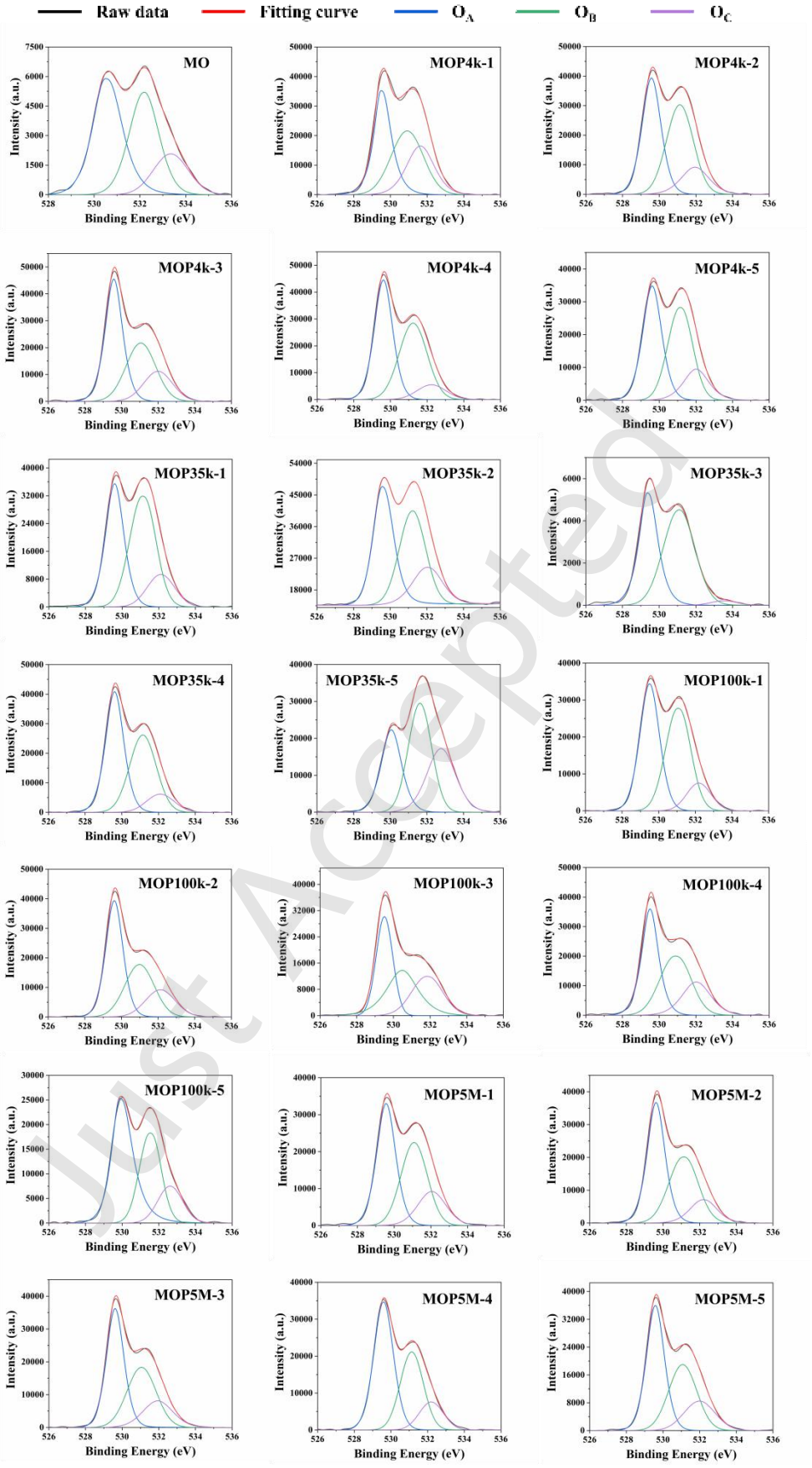

Figure.S8 XPS spectra of pristine InO_x (MO) and PEG-blended films (MOP4k, MOP35k, MOP100k, MOP5M) at different PEG concentrations (1-5 wt%).